fibers

MDPI

Article

Screening Plant-Derived Residues for Bio-Based Construction Materials: A Comparative Physicochemical Characterisation

Brenda Arias-Cárdenas, Ana M. Lacasta *, Laia Haurie and Antonia Navarro-Ezquerra

Department of Architectural Technology, Barcelona School of Building Construction, Universitat Politècnica de Catalunya—Barcelona Tech (UPC), Av. Doctor Marañon 44, 08028 Barcelona, Spain; brenda.arias@upc.edu (B.A.-C.); laia.haurie@upc.edu (L.H.); antonia.navarro@upc.edu (A.N.-E.)

* Correspondence: ana.maria.lacasta@upc.edu

Highlights

What are the main findings?

- Nine of the ten plant-derived residues combined low apparent bulk densities (0.0275–0.1703 g/cm^3) with thermal conductivity values within a narrow range (0.0436–0.0505 W/(m·K)), supporting their potential for lightweight insulation-oriented applications; olive pit was clearly differentiated by substantially higher density and thermal conductivity.
- Posidonia oceanica, rice straw, and sunflower stalk showed particularly balanced profiles for lightweight insulation-oriented development, while Posidonia oceanica and sunflower stalk also exhibited the lowest MCC heat-release parameters.

What are the implications of the main findings?

- The results highlight that residues with similar insulation-related properties can exhibit markedly different combustion-related responses, supporting the value of a multi-property screening approach.
- The proposed comparative screening supports the prioritisation of residues for subsequent material development, while their distinct mineral profiles highlight the need for application-specific compatibility and performance validation.

Abstract

Plant-derived residues are promising renewable feedstocks for bio-based building materials, but their suitability depends on structural, thermophysical, fire-related, and mineral characteristics. This study characterises ten plant residues—corn stalk (CS), hemp stalk (HS), luffa (Lu), olive branches (OB), olive pit (OP), *Posidonia oceanica* (PO), rice husk (RH), rice straw (RS), sunflower stalk (SS), and wheat straw (WS)—to establish a first-stage screening framework for lightweight construction applications. The raw materials were assessed through morphological, density-related, microstructural, thermophysical, thermogravimetric, and microscale combustion analyses, while their calcined fractions were examined by ash-yield determination, X-ray fluorescence, and X-ray diffraction. Apparent bulk density varied by approximately a factor of 30, from 0.0275 g cm^{-3} for RS to 0.8279 g cm^{-3} for OP, while thermal conductivity ranged from 0.0436 to 0.1204 W/(m·K). Most residues remained within the range associated with lightweight insulation, whereas OP showed the highest conductivity. Peak heat release rate (PHRR) ranged from 45.7 W g^{-1} for PO to 145.5 W g^{-1} for Lu, with SS also showing low heat-release parameters. Ash yield varied from 1.66% to 26.23%, accompanied by silica-rich, calcic, alkali-rich, amorphous, and crystalline mineral profiles. The results provide preliminary criteria for categorising and prioritising residues

Check for updates

Academic Editor: Martin J. D. Clift

Received: 11 August 2026
Revised: 29 August 2026
Accepted: 9 September 2026
Published: 14 September 2026

Copyright: © 2026 by the authors. Licensee MDPI, Basel, Switzerland. This article is an open access article distributed under the terms and conditions of the Creative Commons Attribution (CC BY) license.

for lightweight insulation-oriented applications or mineral-related valorisation, as a basis for future composite development and application-level validation.

Keywords: plant-derived residues; bio-based construction materials; material screening; physicochemical characterisation; thermal conductivity; microscale combustion calorimetry; biomass valorisation

1. Introduction

The construction sector is under increasing pressure to reduce its environmental impact and to adopt more resource-efficient and circular material strategies, given its significant contribution to global energy demand and carbon emissions. According to the Global Status Report for Buildings and Construction 2025–2026, the sector accounted for 28% of global energy consumption in 2024 and was responsible for approximately 37% of global CO_2 emissions [1]. Within this context, the search for alternative material resources has intensified, especially those capable of reducing dependence on highly processed and carbon-intensive products. Plant-derived residues have therefore gained growing attention as potential feedstocks for bio-based construction materials, not only because of their renewable origin, but also because they offer an opportunity to valorise biomass streams that are often underused, locally available, and generated in significant quantities [2]. From this perspective, their incorporation into construction materials is increasingly seen as a way to combine waste valorisation, diversification of raw-material sources, and the development of lower-impact building systems, although their suitability depends on the specific structural, thermal, and compositional characteristics of each residue [3].

A wide variety of agro-industrial by-products and other plant-based materials have already been investigated for construction-related applications. Review studies have shown that this interest extends across a wide range of lignocellulosic residues, particularly in relation to thermal insulation and low-impact building products, a context that is also relevant to Euro-Mediterranean regions, where many of these biomass streams are abundant and locally available. In this regard, previous reviews have addressed agro-industrial wastes as potential insulation materials, the use of agro-wastes in Mediterranean building materials, and the broader comparative performance of insulation products for the building sector [4,5].

Among the different families of bio-based resources investigated for construction, plant-derived residues have shown particular promise in non-structural applications, especially when low density, thermal efficiency, and reduced environmental burden are sought [6]. Hemp is one of the best-established examples in bio-based construction and has been widely studied because of its favourable density and acoustic or thermal behaviour in building systems [7–9]. Corn-derived residues have also shown potential for insulation-oriented applications; for example, corn cob has been reported as a promising bio-based material for both thermal and acoustic insulation [10–12]. Olive-related by-products are increasingly being considered within circular bioeconomy and waste-valorisation strategies, and their potential use in construction materials has also been discussed [13,14]. Likewise, bio-based insulation materials based on agricultural residues have been analysed in building-envelope contexts, and rice-derived materials are often identified as particularly relevant because of their abundance and low-density character [15,16]. Together, these studies confirm the broad interest in plant residues for sustainable construction, while also indicating that they have been investigated from different application perspectives and with different levels of characterisation depth.

Despite this growing body of research, comparative studies covering multiple plant residues under a common characterisation framework remain more limited. In many cases, the literature focuses on a single residue, a specific product, or one isolated performance parameter. However, the suitability of a residue for construction cannot be inferred from one property alone. Residues with a similar botanical origin may differ markedly in particle geometry, density, porosity, thermal stability, or mineral fraction, whereas residues from different sources may converge in some properties while diverging strongly in others. For this reason, comparative and multi-technique characterisation is especially valuable when the objective is not only to describe an individual residue, but to distinguish residue-specific material profiles under a common experimental framework [17,18].

In this context, a meaningful comparison among plant residues requires more than the evaluation of a single property. Morphological and density-related analyses are needed to characterise particle geometry, compactness, and internal organisation, which may influence packing, porosity, and the overall physical behaviour of the material. Thermophysical and thermal/fire-related analyses provide complementary information on heat-transfer performance, thermal stability, and combustion-related response, all of which are relevant for bio-based construction materials [3,19]. Taken together, these groups of tests provide a broader basis for identifying material-specific profiles with potential relevance for construction applications and for determining which residue profiles are better aligned with the requirements of lightweight construction materials and related building applications [20].

In this study, ten plant-derived residues were selected for comparative characterisation: corn stalk, hemp stalk, luffa, olive branches, olive pit, *Posidonia oceanica*, rice husk, rice straw, sunflower stalk, and wheat straw. Their selection was based on their availability as agricultural, industrial, or coastal biomass streams, their previous investigation in construction-related materials, and their markedly different supplied or usable morphologies. Previous construction-oriented studies have considered corn and sunflower stalk aggregates or particles and hemp stalk-derived materials in lightweight composites and insulating products [21–23]; rice husk composites, rice-straw particleboards, and wheat-straw insulation boards [24–26]; and olive-pruning waste, olive stones, luffa fibres, and *Posidonia oceanica* fibres in different construction-material configurations [27–29]. Since different particle sizes and degrees of processing have been investigated for these residues, no single morphology can be considered universally representative of their construction-related use. The morphological diversity of the selected set was deliberately preserved rather than eliminated through uniform grinding, as imposing a common particle size could modify structural characteristics relevant to the subsequent use of each residue. However, it is important to consider that particle size and shape influence how the residues arrange within a bulk bed, affecting bulk density, the amount and connectivity of interparticle voids, and the contact between solid elements. Together with the internal pore structure of the particles, these characteristics influence heat transfer through the bed and therefore contribute to properties such as thermal conductivity [30]. Preserving the morphology therefore allows the screening to capture the combined effect of material characteristics and structural arrangement, which may be relevant when selecting residues for subsequent material design. By contrast, a uniform particle size would reduce morphology-related variability and facilitate a more controlled comparison between residues, but could also suppress features such as fibre continuity, particle aspect ratio, or open structural arrangements that may be relevant in construction materials. This diversity was considered especially relevant for determining whether residues sharing a common plant origin nonetheless exhibit clearly differentiated structural, thermal, fire-related, and mineral-related profiles, within a common characterisation framework and for establishing an initial screening of their potential for different bio-based construction applications.

The objective of the present research is therefore to establish a first-stage comparative characterisation framework for plant residues with potential relevance for bio-based construction materials, with particular emphasis on lightweight and insulation-oriented applications. To this end, the plant-derived residues were analysed through particle-related image analysis, apparent bulk density, helium pycnometry, scanning electron microscopy (SEM), thermal conductivity and thermal diffusivity measurements, thermogravimetric analysis (TGA), microscale combustion calorimetry (MCC), and Fourier transform infrared spectroscopy (FTIR). In addition, the ash fractions obtained after calcination were evaluated through ash-yield determination, X-ray fluorescence (XRF), and X-ray diffraction (XRD). By combining these techniques, the study aims to identify the main physical, thermal, combustion-related, and mineral differences among the selected residues, and to determine how their individual property profiles may provide specific advantages or limitations for their potential use in bio-based construction materials. The characterisation is therefore intended to reduce the experimental space associated with the large number of possible residues, binders, formulations, and manufacturing conditions, rather than to demonstrate the final construction performance of the residues. Such performance must subsequently be validated after their incorporation into boards, panels, or other construction-material configurations.

2. Materials and Methods

2.1. Materials

The selection of materials for this study was based on three main criteria: the availability of the residues, their relevance as underutilised biomass streams, and the diversity of their structural and physical characteristics. Most of the selected residues are associated with Mediterranean agricultural or coastal contexts, which makes them especially relevant for construction-oriented research in Southern Europe. At the same time, many of them are linked to agricultural systems that are also widespread internationally, such as rice, maize, sunflower, wheat, hemp, and olive production. This dual condition, namely regional relevance and broader transferability, was considered particularly valuable for assessing residues with both local interest and wider application potential. Luffa was included as a contrasting lightweight biomaterial because, although it is less representative than the other selected residue streams, it is also cultivated on a limited scale in some Mediterranean contexts; its highly open fibrous structure provides a useful counterpoint within the comparative framework and broadens the range of morphologies considered in the study.

The raw materials considered in this study include ten plant-based materials: rice husk (RH), rice straw (RS), olive branches (OB), olive pit (OP), *Posidonia oceanica* (PO), corn stalk (CS), sunflower stalk (SS), luffa (Lu), hemp stalk (HS), and wheat straw (WS). These materials are shown in Figure 1, arranged from left to right and top to bottom.

Where practicable, the residues were characterised in forms representative of their natural occurrence, industrial supply, or previous construction-related use. Rice husk and luffa were analysed in their natural form, while *Posidonia oceanica* was retained in the form in which it was collected. Olive pit was used in the fragmented form supplied by the residue-producing industry. Rice straw, which is generally supplied in large bales, was separated and cut only to the minimum length required for handling and specimen preparation, with the aim of preserving its fibrous morphology and facilitating the transfer of the results to larger specimens. Corn and sunflower stalks were characterised in the shredded forms previously obtained within the SAVASCO project, following the processing route described in [21]. These processed fractions had subsequently been used in construction-related material development [31,32]. Hemp stalk was supplied directly in a commercially shredded form by KANABAT (France) and was used as received, whereas wheat straw

was shredded in the laboratory using a hammer mill (Ercolino 1500 W, Novital, Lonate Pozzolo, Italy). No additional sieving or particle-size selection was performed before characterisation. Different particle sizes, morphologies, and degrees of processing have been reported for plant aggregates and fibres used in construction materials, depending on the residue, manufacturing process, and intended application [33–35]. Assessing multiple particle configurations for each of the ten materials would introduce a substantially larger number of variables and was beyond the scope of the present screening study. Accordingly, one representative form was selected for each residue by prioritising minimum processing and the morphology intended for its subsequent incorporation into lightweight construction materials. A common particle-size distribution was not imposed because uniform grinding would have modified or suppressed morphology-dependent characteristics, such as fibre continuity, open structure, particle geometry, and packing behaviour, which may remain relevant in the intended application. Although standardising particle size would facilitate comparison under a common packing condition, the resulting values would refer to newly imposed particle configurations rather than to the forms selected for practical use. The dimensional, bulk-density, and thermophysical results should therefore be interpreted specifically in relation to the supplied or minimally prepared forms assessed in this study.



Figure 1. Raw plant-derived residues considered in the present study, shown in alphabetical order from left to right and top to bottom: corn stalk (CS), hemp stalk (HS), luffa (Lu), olive branches (OB), olive pit (OP), *Posidonia oceanica* (PO), rice husk (RH), rice straw (RS), sunflower stalk (SS), and wheat straw (WS).

The resulting set covered a broad range of morphologies and residue types, including husk-like and granular residues, elongated fibrous elements, porous lightweight networks, and denser woody by-products. This selection provided contrasting configurations relevant to potential construction applications, ranging from dense fragmented particles to elongated fibres and open three-dimensional networks.

2.2. Methodology

The characterisation of the samples combined complementary techniques aimed at comparing the morphology, physical features, thermal behaviour, fire-related response, and mineral-related composition of the selected plant residues. In order to maintain a coherent comparative approach, the analyses were organised into three main groups: morphological and physical characterisation, thermal and fire-related characterisation, and chemical and mineral characterisation. Because one representative and minimally processed form was selected for each residue, the morphological and physical parameters were interpreted as descriptors of the supplied or prepared forms analysed in this study. These results therefore include the influence of the initial morphology and degree of fragmentation and should not be interpreted as intrinsic properties independent of sample preparation.

2.2.1. Morphological and Physical Characterisation

The first stage of the study focused on the overall morphology and physical configuration of the raw residues. This included particle-related analysis, apparent bulk density, and microstructural observation. Digital image analysis was carried out using the open-source software ImageJ(version: 2.9.0/1.53t)in order to obtain comparative information on particle dimensions, projected area, and dispersion [36]. High-resolution scans of the materials were processed after placing the samples on a black background to maximise contrast and facilitate particle recognition. This analysis was used to assess the relative homogeneity and dimensional variability of the residues, particularly in materials with more particulate morphologies.

Apparent bulk density was determined using an internal comparative procedure. Before testing, all residues were conditioned at 20 ± 5 °C and 60 ± 5% relative humidity. Two separately prepared replicates were tested for each material. The residues were introduced into a rigid cylindrical container with a fixed sample volume of 200 cm^3 and a filling height of 40 mm, corresponding to a nominal internal diameter of approximately 80 mm. The material was gradually poured into the container until the target volume was reached. For residues composed of long, flexible, or resilient fibres, gentle manual rearrangement and settling were applied to place protruding fibres within the container, reduce large visually evident voids, and obtain a sufficiently level and stable upper surface. This procedure was not intended to eliminate the void structure naturally formed by the particles or to achieve a prescribed compacted density. Its purpose was to prevent loosely arranged or protruding fibres from causing excessive deformation of the residue bed during the subsequent placement of the thermal surface probe. No controlled compaction pressure, tapping procedure, or additional external load was applied. All adjustments were completed before weighing, and the prepared beds were not rearranged between the bulk-density and thermal measurements. The apparent bulk density was calculated from the mass of residue contained within the fixed sample volume. Because the packing arrangement depended partly on residue morphology and initial preparation, and only two beds were independently prepared for each material, the resulting apparent bulk-density values should be interpreted as descriptive values obtained under the specified preparation conditions rather than as robust estimates of material variability or as intrinsic properties independent of particle size, orientation, and packing.

Apparent bulk density was used as an indicator of the overall compactness of the different residues. In addition, skeletal density was measured by helium pycnometry using an AccuPyc 1330 pycnometer (version V3.03 1410, Micromeritics Instrument Corporation, Norcross, GA, USA). The analysis was performed on loose material. In combination with the apparent bulk density, this parameter was used to estimate the total porosity of the prepared loose residue beds according to Equation (1):

$$Porosity = 1 - \frac{\rho_{bulk}}{\rho_{skeletal}} \quad (1)$$

where ρ_{bulk} is the apparent bulk density, and $\rho_{skeletal}$ is the skeletal density obtained by helium pycnometry. This density-derived porosity includes the combined contribution of the interparticle voids generated by particle packing and the intraparticle pores accessible to helium. Therefore, it should be regarded as a bulk property of the loose residue bed rather than an intrinsic property of the residue particles. Because particle or envelope density was not independently determined, the interparticle and intraparticle contributions could not be quantified separately. Consequently, the calculated values should not be interpreted as the intrinsic porosity of the individual residue particles, but as the total porosity associated with the tested loose-bed configuration.

The microstructure of the raw residues was then examined by scanning electron microscopy combined with Energy-Dispersive X-ray Spectroscopy (SEM-EDS) in order to identify major structural features such as fibre orientation, internal pore structures and cavities, internal cavities, lamellar organisation, and the relative compactness of the different materials. The images presented in this study were used primarily for comparative morphological assessment of the plant-derived residues. The analyses were performed using a JEOL JSM-6510 scanning electron microscope (JEOL Ltd., Tokyo, Japan) equipped with a Pentafex-INCA EDS detector (Oxford Instruments).

2.2.2. Thermal Characterisation

The thermal characterisation of the raw residues comprised thermal conductivity and diffusivity measurements together with thermogravimetric analysis (TGA) and microscale combustion calorimetry (MCC). Thermal conductivity and diffusivity were measured in order to assess the potential relevance of the residues for lightweight insulating applications. These parameters were used to compare the heat-transfer behaviour of the materials in relation to their structure, apparent bulk density, and packing arrangement. The measurements were performed directly on the same residue beds previously prepared for the apparent bulk-density determination, thereby maintaining the corresponding packing state and a sample thickness of 40 mm. No sealing layer or additional contact material was placed between the sample and the IPS 1105 surface probe. The probe was positioned directly on the prepared upper surface under its own weight, without additional pressure. Because the residue beds were loose and highly porous, perfect contact between the probe and the particles could not always be ensured. This may have added some contact resistance to the measurement. In addition, air movement within the larger and more connected pores may also have contributed to heat transfer. These effects were not measured separately and therefore represent a limitation of the test. Two measurements were carried out for each sample, and the reported values correspond to the average results. The tests were performed using a portable heat transfer analyser ISOMET 2114 (Applied Precision Ltd., Bratislava, Slovakia) equipped with the surface probe IPS 1105 (Applied Precision Ltd., Bratislava, Slovakia), which allows the measurement of thermal conductivity, thermal diffusivity, and volumetric heat capacity [37]. In the context of this study, thermal conductivity was considered the main parameter for comparative assessment, while thermal diffusivity was used as a complementary descriptor of the thermal response of the materials.

TGA was used to evaluate changes in mass as a function of temperature and was considered particularly relevant for comparing the thermal stability of the residues, their decomposition stages, and the amount of solid residue remaining after thermal treatment [38]. The tests were carried out using a NETZSCH STA 449F5 apparatus (NETZSCH-Gerätebau GmbH, Selb, Germany) under a flowing nitrogen atmosphere of 100 mL min^{-1}. The samples were heated from 20 to 800 °C at a rate of 10 °C min^{-1}. The resulting TGA and derivative thermogravimetry (DTG) curves were later used to compare moisture loss, main degradation stages, and final residual mass among the studied residues.

The intrinsic combustion behaviour of the plant-derived residues was further assessed by microscale combustion calorimetry (MCC) using a Microscale Combustion Calorimeter (Concept Equipment Ltd., Worthing, UK), operated in accordance with ASTM D7309 [39]. This technique was used to compare the heat release characteristics of the materials under controlled thermal decomposition and complete combustion conditions, based on the principle of oxygen consumption calorimetry. Small samples with a mass between 1 and 5 mg were placed in the sample holder and heated from ambient temperature to 750 °C at a constant rate of 1 °C s^{-1}, under a nitrogen atmosphere. The decomposition products were then carried into a combustion chamber at approximately 900 °C, where complete oxidation

of the evolved volatiles was achieved. The main parameters obtained from the MCC analysis were the peak heat release rate (pHRR), the temperature at peak heat release rate (TpHRR), the total heat release (THR), and the heat release capacity (HRC), defined as the maximum specific heat release rate divided by the heating rate. The resulting parameters were interpreted as material-level heat-release characteristics under the controlled MCC conditions rather than as direct indicators of ignition or fire behaviour at the scale of a construction product, which would depend on the subsequent composite formulation and application configuration.

2.2.3. Chemical and Mineral Characterisation

Chemical and mineral characterisation combined the analysis of the raw residues by FTIR spectroscopy with the study of their calcined mineral fractions by X-ray fluorescence (XRF) and X-ray diffraction (XRD). This combination made it possible to compare the organic chemical features of the raw materials with the inorganic composition and crystalline phases observed after calcination.

FTIR spectroscopy was used as a complementary technique to identify the main molecular bonds present in the raw residues and to support the interpretation of their lignocellulosic nature. The spectra were examined across the mid-infrared range, and the comparative discussion considered selected bands in both the functional-group and fingerprint regions. [40]. Samples were analysed in powdered form using an attenuated total reflectance (ATR) accessory. Given the comparative scope of the study, FTIR was used primarily to identify common spectral features and general differences among the residues rather than to perform an exhaustive spectroscopic analysis of each material. The analyses were carried out using a Spectrum Two instrument (PerkinElmer, Shelton, CT, USA) operated with Spectrum 1000.02.0009 software.

For the mineral-fraction analyses, representative portions of the raw residues were first oven-dried at 80 °C for 24 h and subsequently calcined from 25 °C at a heating rate of 4.8 °C min^{-1}, with a dwell time of 4 h at the target temperature. Fractions calcined at 600 °C were used for XRD for all residues. For XRF, fractions calcined at 600 °C were analysed for all residues except olive pit (OP), for which calcination at 900 °C was required because the fraction obtained at 600 °C retained excessive residual carbon that prevented adequate fused-bead preparation. This difference was taken into account when interpreting the comparative mineral composition.

The chemical characterisation of the calcined fractions was carried out by X-ray fluorescence (XRF). This technique was used to determine the major oxide composition of the mineral fraction remaining after calcination and to compare the inorganic profiles of the different residues. The quantitative programme included Fe_2O_3, MnO, TiO_2, CaO, K_2O, P_2O_5, SiO_2, Al_2O_3, MgO, and Na_2O. This set of oxides was selected to characterise the major mineral constituents of the biomass ashes and corresponded to the available calibration programme of the instrument. Chlorine and sulphur were not included in the WDXRF quantitative programme, and loss on ignition (LOI) and total organic carbon (TOC) were not independently determined. Consequently, the reported oxide totals represent the sum of the quantified major oxides rather than a complete elemental or mass balance of the ashes. Prior to WDXRF analysis, the calcined fractions were prepared as fused glass beads using a sample-to-flux dilution ratio of 1:20. The fusion procedure was performed at a temperature above 1000 °C and was applied consistently to all samples. The analyses were performed using a sequential wavelength-dispersive X-ray spectrophotometer (WDXRF), specifically a Panalytical Axios PW 4400/40 instrument (PANalytical B.V., Almelo, The Netherlands).

X-ray diffraction (XRD) was used to identify the main crystalline phases present in the calcined fractions obtained at 600 °C for all the samples. The diffractograms were recorded

over a 2θ range from 4 to 100°, with a step size of 0.026° and a measuring time of 200 s. The XRD results were used to complement the XRF data by identifying the main mineral phases associated with each residue after calcination. This qualitative phase identification also allowed the presence of crystalline carbonate-, sulphate-, or chloride-bearing phases not explicitly represented in the major-oxide XRF programme to be assessed. However, XRD was not used to quantify their contribution to the overall ash composition. The analyses were performed using a X'Pert PRO MPD X-ray diffractometer (PANalytical B.V., Almelo, The Netherlands).

3. Results and Discussion

3.1. Morphological and Physical Characterisation

The morphological and physical results refer to the representative supplied or minimally processed form selected for each residue. The particle-related descriptors therefore characterise the tested configurations and should not be interpreted as intrinsic particle dimensions independent of preparation or fragmentation.

Table 1 summarises the main bulk physical and particle-related descriptors obtained for the selected residues, including apparent bulk density, skeletal density, estimated porosity, number of analysed particles, and the mean ± SD and median (IQR) of particle length and width, with a minimum of 100 particles analysed.

Table 1. Apparent bulk density, skeletal density, estimated porosity and particle-related descriptors of the studied plant residues. Particle length and width are reported as mean ± standard deviation (SD) and median (interquartile range, IQR). The IQR was calculated as the difference between the third and first quartiles (Q3 − Q1).

Material	Apparent Bulk Density (g/cm^3)	Skeletal Density (g/cm^3)	Porosity	Number of Particles	Mean Length ± SD (mm)	Median Length (IQR) (mm)	Mean Width ± SD (mm)	Median Width (IQR) (mm)
CS	0.0725	1.6371	0.96	112	13.37 ± 13.85	10.96 (8.39)	3.18 ± 2.53	2.13 (2.40)
HS	0.1703	1.4634	0.88	245	5.86 ± 3.63	4.67 (3.44)	2.16 ± 1.17	1.88 (1.27)
Lu	0.0406	2.0937	0.98	152	6.21 ± 4.36	4.83 (3.41)	2.45 ± 2.28	1.69 (1.74)
OB	0.0667	1.7086	0.96	165	5.62 ± 2.24	5.06 (2.67)	2.33 ± 1.21	2.02 (1.38)
OP	0.8279	1.4006	0.41	880	3.44 ± 0.99	3.20 (1.06)	2.13 ± 0.53	2.03 (0.64)
PO	0.0596	1.5202	0.96	103	17.90 ± 12.86	16.25 (18.75)	6.09 ± 3.79	6.13 (6.72)
RH	0.1372	1.6631	0.92	631	7.43 ± 2.21	7.58 (2.37)	2.38 ± 1.19	2.06 (1.08)
RS	0.0275	1.0565	0.97	102	6.49 ± 2.95	5.42 (2.72)	2.50 ± 1.14	2.41 (0.90)
SS	0.0801	1.3871	0.94	203	8.62 ± 5.42	7.51 (5.10)	2.45 ± 1.59	2.00 (1.49)
WS	0.0895	1.5144	0.94	219	9.14 ± 6.37	7.08 (6.31)	2.64 ± 2.62	1.62 (1.94)

The descriptive coefficient of variation in apparent bulk density, calculated from the two independently prepared residue beds, was below 5% for all materials, indicating close agreement between duplicate preparations under the applied procedure. The density-related results reveal marked differences among the analysed residues and are useful for distinguishing between the apparent compactness of the bulk material and the skeletal density measured for each residue. In terms of apparent bulk density, rice straw, luffa, and *Posidonia oceanica* belong to the lowest-density range, while corn stalk, sunflower stalk, wheat straw, and olive branches occupy an intermediate position. Rice husk and hemp stalk show comparatively higher apparent bulk density within the lightweight residue group. By contrast, olive pit clearly stands out as the densest material of the set, indicating a much more compact arrangement than the rest of the residues.

The comparison between apparent bulk density and skeletal density provides further insight into how this compactness is generated. In residues such as luffa, rice straw, corn stalk, olive branches, and *Posidonia oceanica*, the skeletal density is much higher than the apparent bulk density, resulting in very high estimated porosity values for the prepared

residue beds (0.96–0.98). This indicates that the low apparent density of these materials is mainly associated with a highly open bulk arrangement and a large void fraction related to particle geometry and packing. Rice husk, for instance, combines a still relatively low apparent bulk density with a comparatively high skeletal density, leading to a porosity of 0.92. Olive pit again represents a singular case: although its skeletal density is not the highest of the set, its much higher apparent bulk density results in a markedly lower porosity (0.41), confirming its more compact particulate arrangement. Except for olive pit, the prepared residue beds therefore combine low apparent density with high estimated void fractions, a configuration of interest for lightweight insulation because packing and void content influence their subsequent thermophysical response. Reviews of bio-based insulation materials similarly emphasise the importance of density as one of the key descriptors governing thermal performance and material classification [4,41].

The particle-related descriptors also confirm the morphological diversity of the supplied or minimally prepared forms of the selected materials. *Posidonia oceanica* exhibits the largest mean dimensions, which is consistent with its elongated and heterogeneous fibrous character in the naturally collected form. In contrast, olive pit shows the smallest mean dimensions, in agreement with the compact fragmented form supplied by the residue-producing industry. Rice husk, corn stalk, sunflower stalk and wheat straw occupy intermediate positions, although with clearly different levels of dimensional variability.

The relatively wide dispersion observed for some dimensional parameters reflects the heterogeneous geometries of the representative residue forms selected for this study. The median and IQR values reported in Table 1 provide a complementary description of these distributions, particularly for materials showing broad dimensional variability. The reported means and standard deviations should therefore be interpreted as descriptors of broad morphological distributions rather than as narrowly defined particle-size classes comparable to those obtained for uniformly ground or sieved materials. A box-and-whisker plot summarising the image-derived length and width distributions is presented in Figure 2.

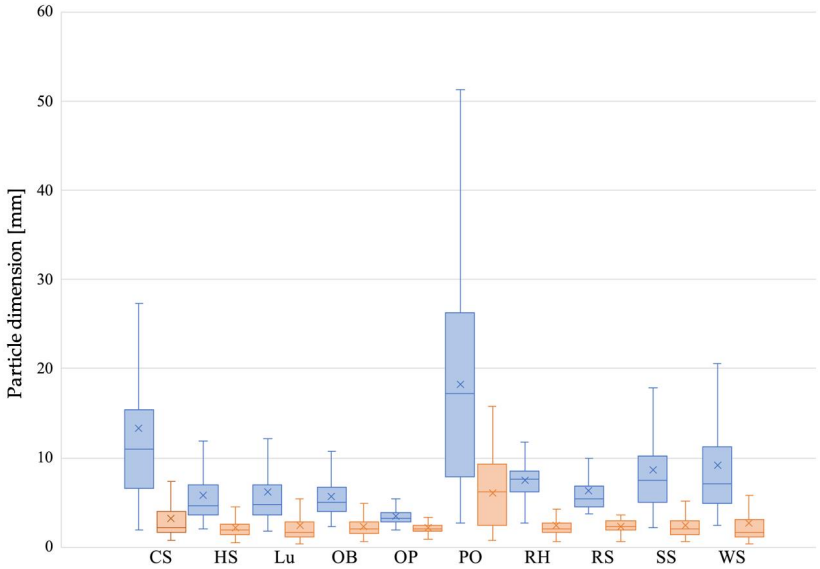


Figure 2. Box-and-whisker plots of particle length (blue) and width (orange) distributions obtained from image analysis for the studied derived-plant residues: corn stalk (CS), hemp stalk (HS), luffa (Lu), olive branches (OB), olive pit (OP), *Posidonia oceanica* (PO), rice husk (RH), rice straw (RS), sunflower stalk (SS) and wheat straw (WS). The horizontal line within each box represents the median, the × symbol indicates the arithmetic mean, the box spans the interquartile range (Q1–Q3), and the whiskers extend to the most extreme values within 1.5 times the interquartile range.

This figure complements the numerical descriptors reported in Table 1 by showing the median, interquartile range, arithmetic mean, and whiskers extending to the most extreme observations within 1.5 times the interquartile range from the corresponding quartile. This dimensional variability is particularly relevant for *Posidonia oceanica* and rice straw, although it has different origins in the two materials. For *Posidonia oceanica*, the broad length distribution reflects the naturally collected material, which contains elongated elements of different dimensions. Rice straw, by contrast, was separated from the supplied bales and cut only as required for handling and specimen preparation. Its measured length therefore reflects this minimal preparation, whereas its width remains more closely associated with the original straw morphology. A similar consideration applies to rice husk. Although the SD values are not negligible, the analysed particles still remain within a comparatively well-defined dimensional domain, which means that the results continue to provide a valid description of the typical size of the husk-derived fragments. In other words, in these cases the dispersion does not simply indicate noise or poor consistency, but rather reflects the morphological nature of the residue and the way in which it is supplied or fragmented. Together with density and porosity, these dimensional descriptors provide an initial indication of how the residues may pack, interlock, or distribute within a future material system, and therefore of the morphology-dependent factors that may affect their subsequent incorporation into bio-based composites. However, because one representative form was selected for each residue, the comparison does not isolate the influence of material composition from that of particle geometry, fragmentation state, and packing arrangement. Overall, Table 1 and Figure 2 confirm that the selected residues do not constitute a homogeneous particulate set, but rather a diverse group ranging from dense fragmented particles to elongated fibrous elements and low-density open structures. The results should consequently be interpreted as a comparison of the supplied or application-oriented forms assessed in this study, rather than as an intrinsic particle-size ranking independent of processing.

SEM-EDS analysis corroborates the diversity of the studied plant-derived residues. Corn stalk (CS), sunflower stalk (SS), and hemp stalk (HS) exhibit longitudinal vascular bundles and porous tissues with small amounts of mineral deposits (Figure 3).

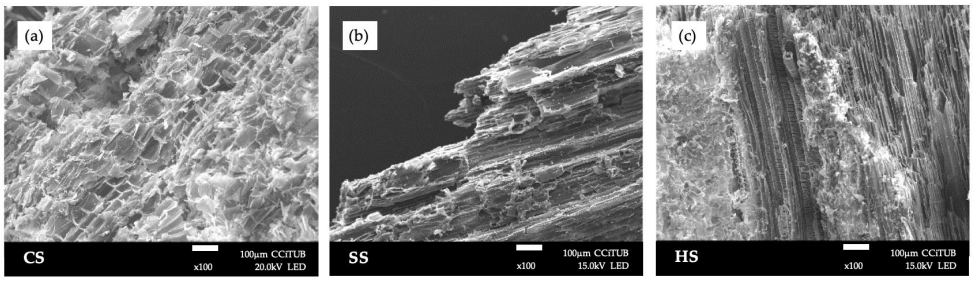


Figure 3. SEM images with 100× magnification showing the fibrous and cellular structure of corn stalk (CS) (**a**), sunflower stalk (SS) (**b**), and hemp stalk (HS) (**c**).

Figure 4 shows the elongated, cellular, porous internal morphology of wheat straw (WS) and rice straw (RS). In both cases, a denser external layer rich in silicon can be observed. The presence of silicon is more remarkable on the epidermis of rice husk (RH), where papillae and silicified trichomes can be distinguished (Figure 4c).

The interconnected network of hollow fibres, with a high content of mineral deposits of Luffa (Lu), can be observed in Figure 5. *Posidonia oceanica* (PO) displays an elongated, fibrous, and laminar morphology. A significant amount of mineral or salt deposits can be distinguished on its surface, which is in good agreement with the EDS identification of considerable amounts of chlorine and sodium (Figure 5a).

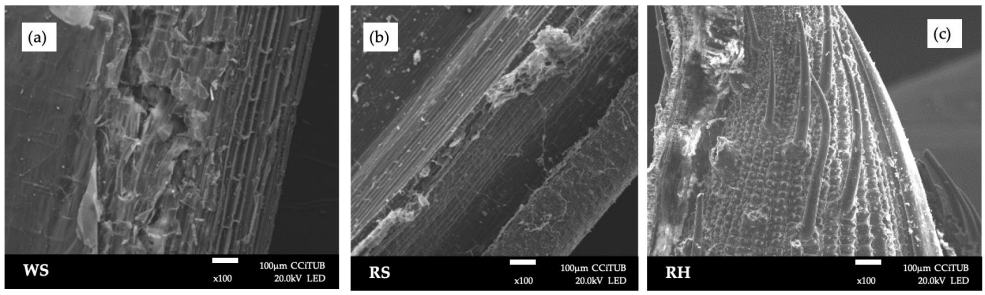


Figure 4. SEM images with 100× magnification showing the elongated, cellular porous internal morphology of wheat straw (WS) (**a**), rice straw (RS) (**b**) and rice husk (RH) (**c**).

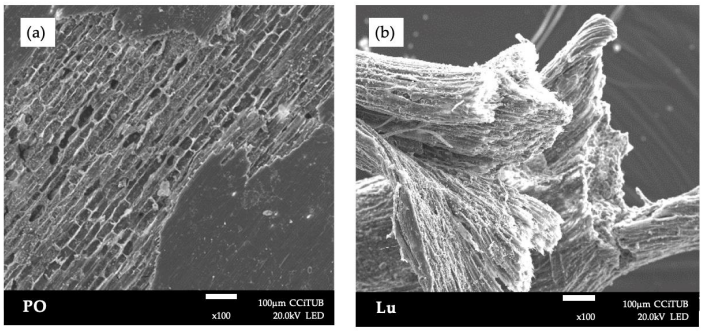


Figure 5. The SEM images at 100× magnification of the external part of the materials, *Posidonia Oceanica* (PO) (**a**) and Luffa (Lu) (**b**).

Figure 6 shows the morphology of the olive branches (OB) and the olive pit (OP). OB consists of woody, irregular fragments with curved or tubular sections. In contrast, the olive pit shows a dense, compact, and granular morphology with little porosity and low mineral contribution.

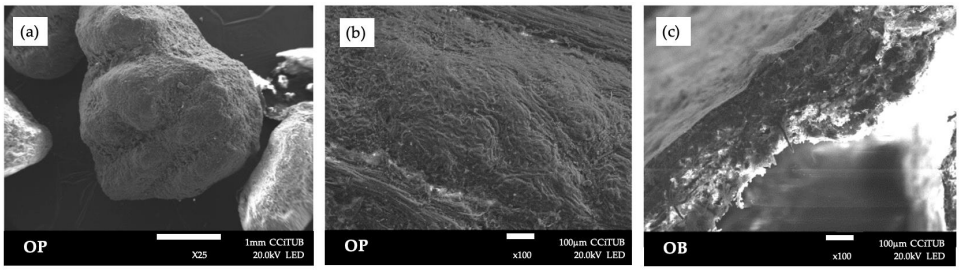


Figure 6. SEM images of the residues: olive pit (OP) (**a**,**b**), showing a dense and compact internal structure, and olive branches (OB) (**c**), showing curved branch-derived fragments with a denser external region and a more heterogeneous fractured inner texture.

3.2. Thermal and Thermophysical Characterisation

This section examines the studied residues from three complementary perspectives: heat-transfer behaviour under steady conditions of the prepared residue beds, assessed through thermal conductivity and diffusivity; thermal stability and degradation behaviour, assessed through thermogravimetric analysis; and combustion-related response, assessed through microscale combustion calorimetry. Together, these parameters provide a broader basis for evaluating the relevance of the residues for lightweight building applications. Apparent bulk density, thermal conductivity, and thermal diffusivity reflect the combined influence of residue composition, selected morphology, degree of fragmentation, and packing arrangement, and should therefore be interpreted in relation to the supplied or prepared forms tested. By contrast, TGA and MCC were conducted on small samples under controlled conditions, and their results can be interpreted as intrinsic material-

level properties under the respective test conditions and are not governed by the initial macroscopic form or packing of the residues.

The thermal conductivity and diffusivity results are summarised in Table 2, along with the density. The analysed residues show very homogeneous behaviour in most cases, with a relatively narrow range of 0.0436–0.0505 W m^{-1} K^{-1}. The only exception is olive pit, which has a much higher thermal conductivity (0.1204 W m^{-1} K^{-1}). This value is consistent with the high density and compact microstructure previously observed for this residue and clearly distinguishes it from the other materials. The lowest conductivity values were obtained for luffa (0.0436 W m^{-1} K^{-1}), rice straw (0.0440 W m^{-1} K^{-1}), and sunflower stalk (0.0440 W m^{-1} K^{-1}). This behaviour is in agreement with the morphological and physical characterisation discussed in Section 3.1 and refers specifically to the representative residue forms and packing conditions assessed in this study.

Table 2. Apparent bulk density, thermal conductivity, and thermal diffusivity for the studied plant-derived residues.

Material	Apparent Bulk Density (g/cm^3)	Thermal Conductivity (W/(m·K))	Thermal Diffusivity (mm^2/s)
CS	0.0725	0.0451	0.4298
HS	0.1703	0.0494	0.3451
Lu	0.0406	0.0436	0.5569
OB	0.0667	0.0505	0.2809
OP	0.8279	0.1204	0.2962
PO	0.0596	0.0455	0.3371
RH	0.1372	0.0477	0.3143
RS	0.0275	0.0440	0.5145
SS	0.0801	0.0440	0.4951
WS	0.0895	0.0458	0.3748

These values are consistent with the ranges commonly reported for thermal insulation materials. In building physics, materials are generally considered thermal insulators when their thermal conductivity is below 0.1 W m^{-1} K^{-1} [42,43], while most insulation materials used in building envelopes under dry conditions typically fall within a narrower range of approximately 0.02–0.07 W m^{-1} K^{-1} [44]. Commercial natural insulation products such as expanded cork and wood fibre boards are commonly reported within the range of 0.036–0.043 W m^{-1} K^{-1} [45,46], whereas reviews of bio-based insulation materials generally report conductivity values between approximately 0.03 and 0.07 W m^{-1} K^{-1}, depending on residue type, density, and processing conditions [47]. Accordingly, with the exception of olive pit, the conductivity values obtained in the present study under the tested packing and probe-contact conditions are within the range expected for lightweight bio-based insulating materials.

Thermal diffusivity followed a less direct pattern, but still provides useful complementary information on the dynamic heat-transfer response of the residues. Since this parameter depends not only on heat conduction but also on the capacity of the material to store thermal energy, it should be interpreted together with conductivity and morphology rather than as an isolated indicator. For this reason, thermal conductivity remains the most direct parameter for comparing the residues from the perspective of thermal insulation.

Termogravimetric analysis (TGA) was used to examine the thermal behaviour of the residues in terms of degradation profile and the amount of solid fraction remaining after heating. Prior to thermal testing, the samples were conditioned at 20 ± 5 °C and 60 ± 5% relative humidity, so the initial mass-loss stage can be interpreted under comparable ambient moisture conditions for all residues. This analysis is particularly relevant in

the present context because it complements the conductivity results by showing how the residues respond to increasing temperature and how much thermally stable material remains after degradation. The corresponding stage-based mass losses and residual masses are shown in Figure 7 and summarised in Table 3.

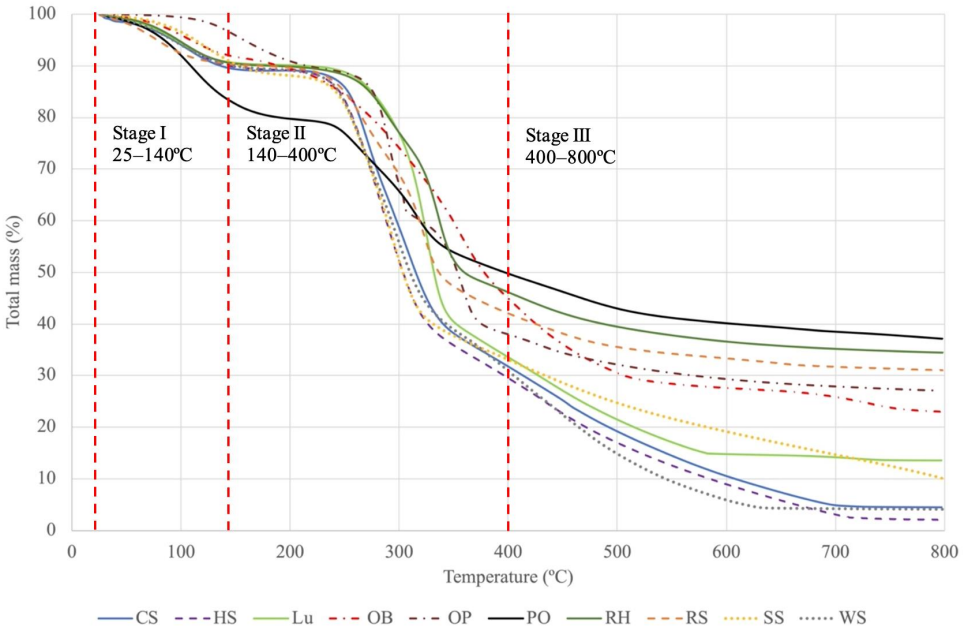


Figure 7. TGA curves of the studied plant residues. The regions delimited with the red dashed lines indicate the three thermal degradation stages considered in this study: Stage I (25–140 °C), mainly associated with moisture release; Stage II (140–400 °C), corresponding to the main pyrolysis region; and Stage III (400–800 °C), associated with additional degradation and residual mass evolution.

Table 3. Mass loss by thermal degradation stage, main DTG peak temperatures in Stages I and II, and residual mass at 800 °C for the studied plant residues. Stage I corresponds to moisture release (25–140 °C), Stage II to the main pyrolysis region (140–400 °C), and Stage III to additional degradation and residual mass evolution (400–800 °C).

Material	Stage I (25–140 °C)		Stage II (140–400 °C)		Stage III (400–800 °C)	
	Mass Loss %	Main DTG Peak (°C)	Mass Loss %	Main DTG Peak (°C)	Mass Loss %	Residual Mass
CS	10.2	107	58	268	27.3	4.5
HS	9.8	105	60.7	279	27.4	2.1
Lu	9.1	100	57.3	325	20	13.6
OB	7.8	107	47.3	349	21.9	23
OP	5.3	140 *	59.3	282	12.8	22.6
PO	16.1	111	34.1	317	12.6	37.1
RH	9.2	102	44.6	335	11.7	34.4
RS	9.5	82	48.4	323	11	31
SS	8.6	112	58.3	294	23	10.1
WS	9.6	97	59.5	298	26.8	4.1

* In OP, the first detected event is shifted towards the upper limit of Stage I.

In agreement with previous studies on lignocellulosic biomass, the degradation process can be interpreted through three main stages: Stage I (25–140 °C), mainly associated with moisture release and low-temperature volatiles; Stage II (140–400 °C), corresponding to the main pyrolysis region; and Stage III (400–800 °C), associated with additional degradation and the evolution of the remaining solid fraction [48,49].

The first stage was relatively limited for most materials, generally ranging from approximately 8 to 10% mass loss. The main exception was *Posidonia oceanica*, which showed a markedly higher loss (16.1%). Since all samples had been conditioned under the same temperature and relative humidity, this result suggests that PO retained more moisture than the other studied residues. By contrast, olive pit showed the lowest first-stage loss (5.3%), indicating a much lower tendency to absorb or retain ambient moisture. This behaviour is consistent with the compact structure previously observed for OP and with the more open and hygroscopically responsive morphology identified for PO.

The most significant degradation occurred during Stage II, where the residues showed their main thermal decomposition. The highest mass losses in this interval were observed for hemp stalk (60.7%), wheat straw (59.5%), olive pit (59.3%), and sunflower stalk (58.3%), indicating that a large proportion of their mass was degraded within the main pyrolysis region. By contrast, lower values were obtained for *Posidonia oceanica* (34.1%), rice husk (44.6%), and olive branches (47.3%), suggesting a greater relative contribution of thermally stable or non-volatile fractions in these materials. The main derivative thermogravimetry (DTG) peaks in this interval were generally located between 268 and 349 °C. This temperature range is consistent with those commonly reported for the main degradation of hemicellulose- and cellulose-rich lignocellulosic fractions [49–51].

The differences became even more evident in Stage III and in the final residual mass. *Posidonia oceanica* (37.1%), rice husk (34.4%), and rice straw (31.0%) showed the highest residual masses at 800 °C, whereas hemp stalk (2.1%), wheat straw (4.1%), and corn stalk (4.5%) left only a limited solid residue. These differences indicate that the studied residues vary not only in the extent of their organic degradation, but also in the proportion of thermally stable or mineral-related matter remaining after heating.

Overall, the TGA results confirm that the studied residues share the general three-stage degradation pattern typical of lignocellulosic biomasses, but differ markedly in the extent of moisture-related mass loss, the intensity of the main degradation stage, and, most clearly, in the amount of solid residue retained after heating. Residues such as *Posidonia oceanica*, rice husk, and rice straw showed comparatively high residual masses, whereas hemp stalk, wheat straw, and corn stalk left only a limited solid fraction at the end of the test. This indicates that the thermal response of the studied residues cannot be interpreted only in terms of degradable organic matter, but must also consider the contribution of more thermally stable and mineral-related fractions.

To complement the thermogravimetric analysis, the intrinsic combustion behaviour of the residues was further assessed by microscale combustion calorimetry (MCC). This technique provides a comparative characterisation of the combustion properties and intrinsic flammability of the materials at the microscale. The most relevant parameters are the peak heat release rate (PHRR), the temperature at peak heat release (TpHRR), the total heat release (THR), the heat release capacity (HRC), and the residual yield after combustion. For comparative purposes, lower PHRR, THR, and HRC values indicate a lower combustion hazard, whereas higher residual yield reflects a greater fraction remaining after combustion. In addition, a lower TpHRR indicates that the material reaches its maximum heat release at a lower temperature, suggesting an earlier development of the main combustion event. The corresponding results are summarised in Table 4. HRC is particularly useful in this context, as it is widely regarded as one of the most informative MCC-derived indicators of intrinsic flammability at microscale [52].

The MCC results revealed marked differences among the studied residues. The most favourable overall profiles were observed for *Posidonia oceanica* and sunflower stalk, which showed the lowest PHRR values, 45.7 and 46.4 W g^{-1}, respectively, together with low THR values (4.0 and 4.6 kJ g^{-1}) and low HRC values (33.6 and 41.0 J g^{-1} K^{-1}). These

results indicate a lower combustion risk under the conditions of the MCC test. Rice straw, olive pit, and wheat straw occupied an intermediate position, with THR values between 6.0 and 7.4 kJ g^{-1} and PHRR values between 74.4 and 99.4 W g^{-1}. By contrast, luffa showed the highest PHRR value (145.5 W g^{-1}), together with high THR (9.7 kJ g^{-1}) and HRC (81.0 J g^{-1} K^{-1}), which is consistent with the steepest mass-loss rate observed in the TGA curves. Hemp stalk and corn stalk also showed comparatively elevated combustion-related parameters, with PHRR values of 109.1 and 90.3 W g^{-1} and THR values of 9.1 and 8.0 kJ g^{-1}, respectively.

Table 4. Microscale combustion calorimetry parameters of the studied plant residues: peak heat release rate (PHRR), temperature at peak heat release (TpHRR), total heat release (THR), heat release capacity (HRC), and residual yield (Yc).

Material	PHRR (W/g)	TpHRR (°C)	THR (kJ/g)	HRC (J/g·K)	Residue Yc (%)
CS	90.3	357	8.0	72.0	19.4%
HS	109.1	352	9.1	85.5	17.8%
Lu	145.5	389	9.7	81.0	20.0%
OB	66.6	372	12.6	106.0	20.3%
OP	96.1	362	7.4	72.4	20.7%
PO	45.7	337	4.0	33.6	24.7%
RH	88.3	369	7.6	61.5	31.4%
RS	74.4	341	6.9	59.7	28.0%
SS	46.4	324	4.6	41.0	32.9%
WS	99.4	348	6.0	80.2	22.7%

Olive branches showed a distinctive profile. Although their PHRR remained moderate (66.6 W g^{-1}), they exhibited the highest THR (12.6 kJ g^{-1}) and the highest HRC (106.0 J g^{-1} K^{-1}) among the studied residues. This is consistent with the broader combustion peak observed in the MCC curve, indicating that heat release was distributed over a wider temperature interval rather than concentrated in a sharp maximum. Rice husk also showed comparatively elevated combustion-related parameters, with PHRR of 88.3 W g^{-1}, THR of 7.6 kJ g^{-1}, and HRC of 61.5 J g^{-1} K^{-1}, placing it above residues such as rice straw or sunflower stalk but below luffa, hemp stalk, or olive branches in overall heat-release terms.

The temperature at peak heat release (TpHRR) ranged from 324 °C for sunflower stalk to 389 °C for luffa. In comparative terms, a lower TpHRR indicates that the main combustion event reaches its maximum at a lower temperature under the imposed MCC heating programme. Accordingly, residues such as sunflower stalk, *Posidonia oceanica*, and rice straw reached their combustion maximum at lower temperatures, whereas luffa, olive branches, and rice husk required higher temperatures for the main combustion event to develop fully. Although this parameter provides useful information on the temperature at which the main combustion event occurs, it should be interpreted together with PHRR, THR, and HRC rather than as an isolated indicator. Importantly, TpHRR does not represent an ignition temperature or ignition time, which were not determined in the present MCC test. In addition, the residual yield after combustion also differed among materials, with sunflower stalk and rice husk showing the highest values, followed by rice straw and *Posidonia oceanica*, whereas hemp stalk and corn stalk left comparatively lower residues. In the present study, the comparative interpretation of MCC is therefore based primarily on the intensity of heat release, the total energy released, the residual yield after combustion, and the temperature at which the main combustion event occurs.

From a broader interpretative perspective, MCC adds a complementary layer of information to TGA because it not only indicates how much mass is lost, but also how energetically the evolved volatiles are combusted. This is especially useful in the present

study because residues with relatively similar thermal conductivity or even comparable TGA residues may still differ substantially in their MCC response, as illustrated by the contrast between materials such as *Posidonia oceanica*, rice husk, and luffa. In this sense, MCC helps distinguish between residues that are thermally stable because they retain a large solid fraction and those whose volatile fraction is intrinsically more or less energetic during combustion. At the same time, as highlighted in the literature, MCC is widely used as a comparative screening method for assessing material-level heat-release characteristics under controlled conditions. In this context, its value lies in enabling a consistent differentiation among materials, particularly when residues with relatively similar TGA residue or thermophysical behaviour still show clearly different combustion-related responses. Reported relationships between MCC parameters and larger-scale calorimetric tests are not uniform, but rather depend on the specific parameter considered. Moreover, macroscopic fire behaviour, including ignition time, is influenced by additional factors such as density, porosity, packing, specimen thickness and thermal properties and, in composite systems, by the nature and amount of binder. Such application-level behaviour cannot therefore be predicted from MCC data alone and would need to be evaluated once the composite formulation and product configuration have been defined. MCC is therefore especially useful here as a complementary method within the comparative framework adopted in this study, since it adds combustion-related information that cannot be inferred from TGA alone [53,54].

Thermal conductivity and diffusivity describe the heat-transfer response of the prepared residue beds, whereas TGA and MCC characterise material-level degradation and combustion behaviour under their respective test conditions. Apparent bulk density provides an additional descriptor of the physical configuration of the residue bed, reflecting the amount of solid material contained within a given bulk volume and, together with particle morphology, the way in which the particles are arranged. In loose residue beds, a lower bulk density can be associated with a more open particle arrangement, which may facilitate gas transport through the material. However, bulk density does not directly quantify oxygen accessibility, since gas transport also depends on factors such as particle size and shape and the connectivity of the void space. Thermal conductivity introduces a further consideration: a low conductivity limits conductive heat transfer away from a locally heated region and may therefore favour local heat accumulation, while simultaneously reducing heat penetration towards adjacent material. Consequently, neither apparent bulk density nor thermal conductivity alone can be interpreted as an indicator of fire behaviour. Their combined interpretation with the MCC-derived heat-release parameters instead provides a multidimensional screening of the thermal and combustion-related characteristics of the residues. To facilitate this combined screening, Figure 8 integrates apparent bulk density, thermal conductivity and the MCC-derived THR and HRC parameters in a single representation. Thermal conductivity is plotted against apparent bulk density, while bubble size represents THR and colour represents HRC. This representation allows residues with comparable insulation-related behaviour but contrasting heat-release characteristics to be readily distinguished, without implying a direct classification of their fire performance at product scale.

Most residues occupy a relatively narrow thermal-conductivity range despite showing substantially different MCC responses. Lu combines low apparent bulk density and low thermal conductivity with the highest HRC and a comparatively high THR, indicating a favourable insulation-related response but a less favourable microscale heat-release profile within the materials studied. By contrast, *Posidonia oceanica* and sunflower stalk combine low thermal conductivity with comparatively low THR and HRC. Olive pit remains clearly differentiated by its substantially higher apparent bulk density and thermal conductivity.

Overall, the combined representation reveals trade-offs between insulation-related and combustion-related characteristics and provides preliminary criteria for selecting residues for subsequent composite development and application-level validation.

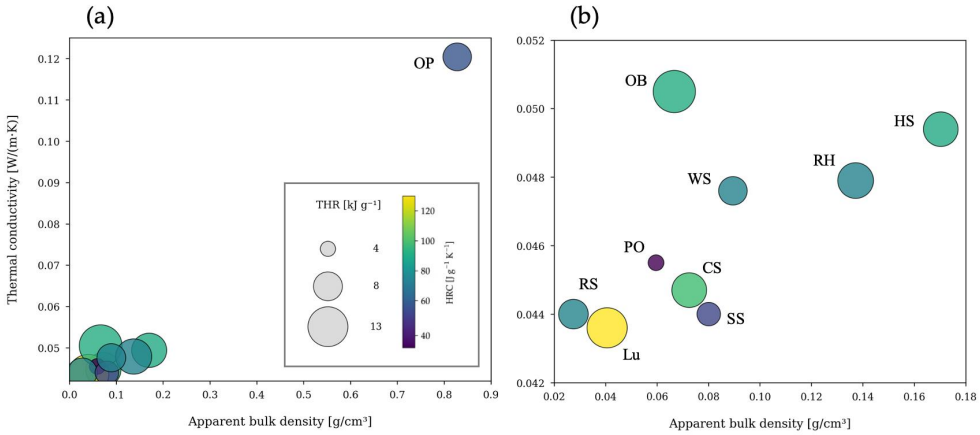


Figure 8. Integrated comparison of apparent bulk density, thermal conductivity, and MCC-derived heat-release parameters for the studied plant residues. Apparent bulk density is represented on the *x*-axis and thermal conductivity on the *y*-axis, while bubble size represents total heat release (THR) and bubble colour represents heat release capacity (HRC). (**a**) Full data range including all residues; (**b**) enlarged view of the low-density region to facilitate comparison among the lightweight residues.

3.3. Chemical and Mineral Characterisation

The chemical and mineral characterisation was undertaken to complement the morphological, physical, and thermal analyses previously discussed, and to provide additional insight into the intrinsic composition of the studied residues. In this context, the plant-derived residues were first examined by FTIR in order to identify their main organic functional features, whereas the mineral fraction obtained after calcination was subsequently analysed in terms of ash yield, major oxide composition, amorphous content, and crystalline phases. This combined approach makes it possible to relate the lignocellulosic nature of the residues to the inorganic fraction remaining after thermal treatment, thereby providing a broader basis for interpreting their potential behaviour in bio-based building applications.

The FTIR spectra of the raw residues confirmed the lignocellulosic nature of the studied biomasses, while also revealing differences in the relative intensity and definition of several absorption bands. In the present study, FTIR was therefore used as a comparative technique to assess how the main organic functional groups were expressed in each residue rather than to provide an exhaustive spectroscopic assignment of every individual peak [49,55–58]. For clarity, the main spectral differences are discussed here by defined spectral areas, as indicated in Figure 9.

All materials showed the characteristic bands commonly associated with plant-derived lignocellulosic residues. These include a broad absorption in the hydroxyl region, bands related to aliphatic C–H vibrations, and several signals in the fingerprint region associated with cellulose, hemicellulose, lignin, and related functional groups. However, the relative development of these bands was not equivalent among materials, indicating that, although all residues share a common organic basis, their chemical profiles are not identical.

In Zone 1, corresponding to approximately 3368–3301 cm^{-1}, all materials exhibited a broad band associated with O–H stretching vibrations, generally related to hydroxyl groups in cellulose, hemicellulose, lignin, and absorbed moisture. This band was particularly marked in *Posidonia oceanica* (PO), suggesting a stronger contribution of polar functional

groups and a higher affinity for moisture. This interpretation is consistent with the higher initial mass loss previously observed for PO during TGA.

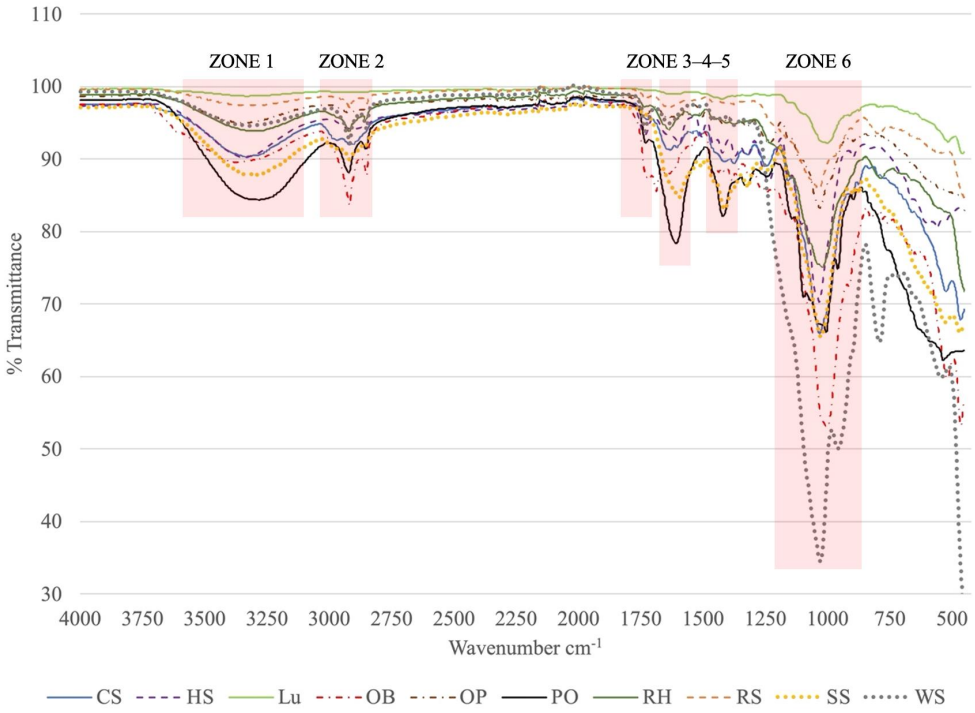


Figure 9. FT-IR graphic analysis of the plant-derived residues indicates the wavenumber range at the peaks. The merged shaded area labelled "ZONE 3-4-5" is a graphical simplification representing three non-continuous intervals: Zone 3 (1687–1590 cm^{-1}), Zone 4 (1414–1365 cm^{-1}), and Zone 5 (1243–1234 cm^{-1}).

In Zone 2, around 2926–2902 cm^{-1}, the spectra showed the expected C–H stretching vibrations of aliphatic groups, characteristic of lignocellulosic structures. Although this band was present in all residues, it appeared more clearly defined in olive branches (OB) and *Posidonia oceanica* (PO), indicating a stronger expression of aliphatic C–H vibrations in these materials. In Zone 3, approximately 1687–1590 cm^{-1}, the observed bands may be associated with carbonyl and/or aromatic skeletal vibrations, depending on the relative contribution of lignin-related structures.

The fingerprint region showed the most relevant differences among residues. In Zone 4, around 1414–1365 cm^{-1}, the band was particularly marked in *Posidonia oceanica* (PO), suggesting a stronger contribution of CH deformation and/or O–H bending vibrations in this region. In Zone 5, between approximately 1243 and 1234 cm^{-1}, the absorptions are commonly associated with C–O and C–O–C vibrations linked to lignin and hemicellulosic components, and were more clearly expressed in *Posidonia oceanica* (PO) and wheat straw (WS). Taken together, Zones 3–5 indicate that the residues do not present the same relative balance between cellulose-, hemicellulose-, and lignin-related contributions, even though all of them remain within the broader lignocellulosic family.

The most distinctive differences were observed in Zone 6, between approximately 1038 and 904 cm^{-1}, where the spectra showed strong absorptions typically associated with C–O and C–O–C vibrations in polysaccharides, especially cellulose and hemicellulose. This area was particularly intense in wheat straw (WS) and also clearly marked in olive branches (OB), indicating a strong expression of oxygenated organic vibrations in this region. By contrast, luffa (Lu) and rice husk (RH) showed smoother or less sharply differentiated profiles, confirming that the residues differ not only in physical structure and thermal behaviour, but also in the way their main oxygenated organic groups are expressed.

The spectral differences indicate variations in the relative expression of the principal lignocellulosic functional groups, which may affect subsequent interactions with moisture or binders. The analysis was then extended to the amount and composition of the inorganic fraction remaining after calcination.

Before discussing the major oxide composition of the calcined residues, the ash yield obtained after calcination at 600 °C provides a first indication of the relative inorganic fraction associated with each material. In general, the ash-yield results were qualitatively consistent with the TGA trends. *Posidonia oceanica* showed the highest ash yield (26.23%), followed by rice husk (15.05%) and rice straw (11.15%), whereas hemp stalk remained low (2.87%). The main exception was olive pit, which showed the lowest ash yield (1.66%) despite its comparatively high TGA residue, indicating a stronger tendency for char formation under inert conditions than a high mineral fraction. In this way, ash yield provides a useful link between the thermal behaviour discussed above and the inorganic composition analysed by XRF.

The XRF results, summarised in Figure 10, reveal a marked variability in the quantified major-oxide composition among the studied residues, confirming that the differences previously suggested by ash yield and FTIR also extend to the inorganic composition of the calcined fraction. The percentages discussed below refer exclusively to the ten major oxides included in the XRF calibration programme and should therefore not be interpreted as a complete mass balance of the ashes. From a comparative perspective, the ashes can be grouped into three main compositional tendencies: silica-dominated residues, residues with stronger calcic or silico-calcic contributions, and residues characterised by higher alkali contents.

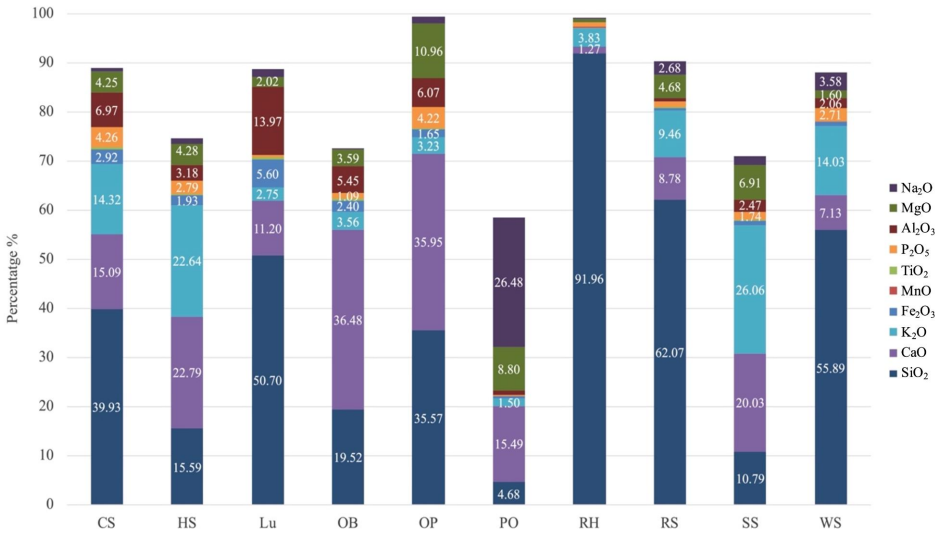


Figure 10. Quantified major-oxide composition of the ash fractions obtained after calcination at 600 °C for the studied plant-derived residues, as determined by XRF.

The clearest silica-rich residue is rice husk, whose ash is overwhelmingly dominated by SiO_2 (91.96%), with only minor contributions from the remaining oxides. Rice straw and wheat straw also showed clearly siliceous ashes, with SiO_2 contents of 62.07% and 55.89%, respectively. These three residues therefore define the most clearly silica-dominated subgroup within the studied set. In the same general direction, luffa and corn stalk also exhibited silica as the dominant oxide, although with a much more mixed composition. In particular, luffa combined SiO_2 (50.70%) with a relevant CaO fraction (11.20%) and comparatively high Al_2O_3 (13.97%), whereas corn stalk showed a more balanced profile between SiO_2 (39.93%), CaO (15.09%), and K_2O (14.32%). This indicates that, although

silica remained the major component in both cases, their ash fractions were less chemically concentrated than those of the rice-derived residues.

A second group is represented by residues with a stronger calcic contribution. Olive branches were dominated by CaO (36.48%), followed by SiO_2 (19.52%), whereas olive pit showed a distinctly silico-calcic composition, with very similar proportions of SiO_2 (35.57%) and CaO (35.95%), together with a relevant contribution of MgO (10.96%). Taken together, these results distinguish the olive-derived ashes from the more silica-dominated agricultural residues and confirm their more mixed mineral character. However, the OP XRF results should be interpreted with caution because this fraction was calcined at 900 °C rather than 600 °C. Although all samples subsequently underwent the same high-temperature fused-bead preparation, the higher calcination temperature used for OP may have caused some additional mass loss or volatilisation of more volatile species before analysis. Therefore, minor differences in the relative oxide proportions compared with a fraction pre-calcined at 600 °C cannot be excluded.

The most alkali-rich profiles were observed in hemp stalk, sunflower stalk, and particularly *Posidonia oceanica*. In hemp stalk, the ash was dominated by K_2O (22.64%) and CaO (22.79%), while sunflower stalk showed a similar but even more K-rich profile, with K_2O reaching 26.06% and CaO 20.03%. *Posidonia oceanica* was the most distinctive case, with a very low SiO_2 content (4.68%) but high proportions of Na_2O (26.48%), CaO (15.49%), and MgO (8.80%). This clearly differentiates PO from the agricultural residues and is coherent with its marine origin. Within the comparative set, PO therefore represents the most singular inorganic profile, clearly separated from both the silica-rich residues and the more calcic woody subgroup.

It is worth noting that, for some samples, the total sum of the ten major oxides quantified by XRF did not reach 100%. These totals should not be interpreted as a complete mass balance of the ashes because chlorine and sulphur were not quantified and LOI was not independently determined. In addition, biomass ashes produced at 600 °C may contain residual carbon together with carbonate-, chloride- or sulphate-bearing phases that are not fully represented when the detected elements are conventionally reported as oxide equivalents [20,59]. Consequently, the difference between the sum of the quantified oxides and 100% was considered an unquantified fraction and was not assigned directly to loss on ignition or interpreted as an analytical inconsistency. The XRF results were therefore reported without normalisation to 100%.

From a comparative point of view, the XRF results confirm that the mineral fraction of the studied residues is qualitatively distinct in terms of its quantified major-oxide distribution, in addition to the differences in ash yield described above. In practical terms, this means that residues with similarly low density or similarly low thermal conductivity may still differ substantially in the composition of the ash fraction generated after calcination. This variability is particularly relevant because it suggests that the residues may behave differently not only during thermal treatment, but also in later interactions with binders, coatings, or other mineral phases within bio-based construction systems.

While XRF provided information on the major-oxide profiles of the ash fractions, it did not identify the mineral phases in which these elements were present. For this reason, the calcined residues at 600 °C were further analysed by X-ray diffraction (XRD), in order to characterise their crystalline phases. The XRD interpretation considered both the relative amorphous or crystalline character of each ash and its principal mineral phases, thereby allowing the oxide profiles to be related to the corresponding mineral assemblages. The main phase assignments are indicated in Figure 11, while the following discussion focuses on the phases most relevant to distinguishing the residues and interpreting their XRF profiles. The identification of phases containing constituents not included in the ten-oxide

XRF programme also assisted in the qualitative interpretation of some oxide totals below 100%. However, as the XRD analysis was qualitative, the identification of a phase does not indicate its abundance or quantify its contribution to the unquantified fraction.

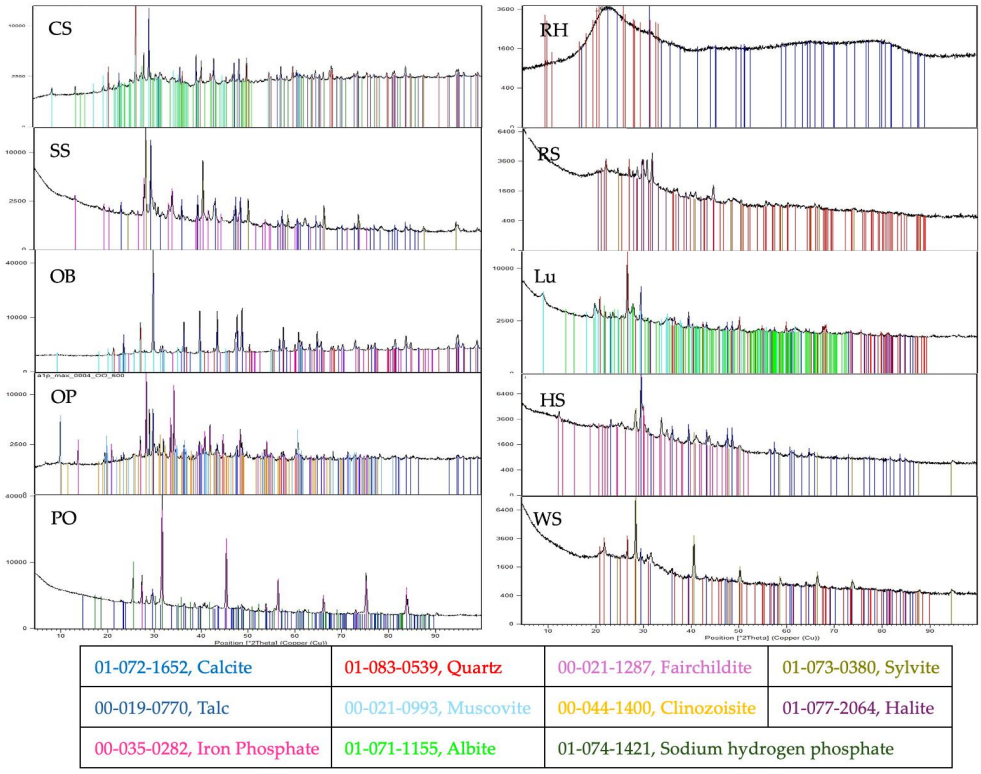


Figure 11. XRD patterns of the ash fractions obtained after calcination at 600 °C, showing the mineralogical variability and the principal crystalline phases identified in the studied plant-derived residues.

The diffractograms revealed marked differences not only in crystallinity but also in mineral assemblage. Rice husk (RH) displayed the most predominantly amorphous pattern, with a broad diffuse pattern and only limited crystalline reflections. This behaviour is consistent with the very high SiO_2 content determined by XRF and indicates that silica remained mainly in a poorly ordered form at 600 °C. Rice straw (RS) also showed a substantial diffuse contribution, but with a larger number of superimposed reflections, including quartz, sylvite (KCl), and sodium phosphate, corresponding to a mixed amorphous–crystalline siliceous fraction. Thus, although both rice-derived residues were silica-rich according to XRF, their mineral organisation after calcination was not equivalent, since RS has a potassium salt (sylvite) which is not found in RH.

At the other end of the spectrum, *Posidonia oceanica* (PO), olive branches (OB), olive pit (OP), corn stalk (CS) and sunflower stalk (SS) exhibited diffractograms with numerous sharp and well-resolved reflections, indicating that their ash fractions were already clearly crystalline at 600 °C. Despite this common crystalline character, their phase assemblages were markedly different. Among these materials, PO was particularly distinctive, showing a highly resolved pattern that was coherent with its high ash yield and its differentiated XRF profile, characterised by low silica and high Na-, Ca-, and Mg-related contents. The identified phases included calcite, halite, and sodium phosphate. The presence of halite (NaCl) indicates that chloride-bearing salts formed part of the mineral fraction. Their presence is particularly relevant for construction applications because soluble chloride-bearing salts may affect cement hydration and, in reinforced cementitious systems, increase the risk of chloride-induced steel corrosion [60–62]. The associated Na contribution may also

increase the alkali loading of the system, which can be relevant when reactive aggregates are present. Consequently, the soluble chloride and alkali content and their compatibility with the intended binder should be assessed before using PO in cement-based or alkali-activated systems. Since chlorine was not included in the XRF quantitative programme, these phases provide a plausible qualitative explanation for part of the particularly large unquantified fraction observed for PO. The identification of calcite additionally indicates a carbonate contribution, consistent with its Ca-rich mineral profile.

The olive-derived residues (OB and OP) were characterised by carbonate-rich mineral assemblages. OB contained calcite, quartz, and muscovite, whereas OP contained calcite and fairchildite as carbonate phases, together with talc and clinozoisite. Sunflower stalk (SS) also showed abundant carbonate phases, including calcite, sylvite, and fairchildite, in agreement with its elevated CaO and K_2O contents. Corn stalk (CS) exhibited a more heterogeneous assemblage composed of quartz, calcite, and aluminosilicate phases (muscovite and albite), consistent with its balanced Si-, Ca-, K-, and Al-related oxide composition.

Hemp stalk (HS), luffa (Lu), and wheat straw (WS) occupied an intermediate position between the predominantly amorphous rice residues and the highly crystalline ashes described above. Their diffractograms combined diffuse backgrounds with well-defined crystalline reflections, indicating mixed mineral assemblages. HS contained calcite, sylvite (KCl), and iron phosphate. Lu contained calcite and quartz, together with the aluminosilicate phases muscovite and albite. WS combined a partially amorphous siliceous fraction with crystalline quartz, calcite, and sylvite (KCl). The occurrence of sylvite in HS and WS indicates the presence of a chloride-containing salt not represented in the major-oxide XRF programme.

From a comparative perspective, the main value of the XRD analysis in this study lies in confirming that the calcined residues cannot be treated as a single ash family. Instead, they show clearly differentiated mineral organisations: from predominantly amorphous ash fractions, as in RH, to strongly crystalline residues such as PO and the olive-derived materials, with several intermediate cases in between. XRD therefore complements ash yield and XRF by showing that the mineral fractions differ not only in quantity and major-oxide composition, but also in structural organisation and mineral assemblage. In terms of construction applications, the presence of a more amorphous fraction may suggest a greater potential for pozzolanic-type reactivity, whereas more crystalline fractions are generally associated with lower reactivity and greater mineral stability. However, the potential behaviour of the ashes also depends on the specific phases present rather than on crystallinity alone. For example, silica-rich amorphous fractions, stable carbonate minerals, and soluble chloride-bearing salts may have different implications for reactivity, compatibility, and durability in mineral-based systems. As no direct reactivity or application-performance tests were conducted, the results provide a mineralogical screening rather than evidence of suitability for a specific valorisation route.

3.4. Comparative Synthesis of the Studied Residues

A comparative overview of the main results is presented in Table 5. The comparison is based on one representative form selected for each residue, prioritising minimum processing, practical availability, and the morphology intended for its subsequent construction-related use. Consequently, the morphology, apparent bulk density, estimated porosity, thermal conductivity, and thermal diffusivity results should be interpreted in relation to the supplied or prepared forms tested, whereas the TGA and MCC results describe material-level behaviour under their respective controlled test conditions. The combined characterisation shows that the studied residues should not be interpreted as a single homogeneous biomass group, but rather as a set of materials with clearly differentiated balances between

structure, thermophysical response, and chemical/mineral fraction. Although all residues share a broadly lignocellulosic basis, the results reveal marked differences in morphology, bulk and skeletal density, estimated porosity, thermal conductivity, thermal degradation, microscale combustion response, ash yield, and mineral fraction after calcination.

Table 5. Comparative synthesis of the main physical, thermophysical, fire-related, and chemical/mineral characteristics of the studied plant residues, highlighting their overall screening profile for potential bio-based construction applications.

Vegetal Residue	Morphological and Physical Characterisation	Thermal Conductivity [W m^{-1} K^{-1}]	Thermal Degradation and Combustion-Related Response	Ash and Mineral-Fraction Characterisation	Potential/Possible Construction-Oriented Use
CS	Bulk density: 0.0725 g cm^{-3}; porosity: 0.96 (high); elongated stalk-derived particles	0.0451	TGA residue: 4.5%; PHRR: 50–100 W g^{-1}; TpHRR: >350 °C	Ash yield: 7.97%; ash: mixed siliceous–calcic; crystalline	Potential for lightweight insulating composites
HS	Bulk density: 0.1703 g cm^{-3}; porosity: 0.88; fibrous particles	0.0494	TGA residue: 2.1%; PHRR: >100 W g^{-1}; TpHRR: >350 °C	Ash yield: 2.87%; ash: alkali/calcic; mixed	Possible use in lightweight fibrous composites, though less suitable for insulation-oriented screening
Lu	Bulk density: 0.0406 g cm^{-3} (low); porosity: 0.98 (high); highly open fibrous network	0.0436	TGA residue: 13.6%; PHRR: >100 W g^{-1}; TpHRR: >350 °C	Ash yield: 14.09%; ash: silica-rich; mixed amorphous–crystalline	Strong interest for lightweight insulation-oriented uses, with combustion-related behaviour to be considered
OB	Bulk density: 0.0667 g cm^{-3}; porosity: 0.96 (high); woody irregular fragments	0.0505	TGA residue: 23.0%; PHRR: 50–100 W g^{-1}; TpHRR: >350 °C	Ash yield: 12.90%; ash: calcic; crystalline	Possible interest as woody filler/reinforcement or for differentiated mineral-related applications
OP	Bulk density: 0.8279 g cm^{-3} (high); porosity: 0.41 (low); compact granular morphology	0.1204	TGA residue: 22.6%; PHRR: 50–100 W g^{-1}; TpHRR: >350 °C	Ash yield: 1.66%; ash: silico-calcic; crystalline	Not suitable for lightweight insulation; possible interest for dense filler/reinforcement or differentiated valorisation routes
PO	Bulk density: 0.0596 g cm^{-3}; porosity: 0.96 (high); elongated fibrous/laminar morphology	0.0455	TGA residue: 37.1%; PHRR: <50 W g^{-1}; TpHRR: <350 °C	Ash yield: 26.23% (high); ash: alkali- and Ca-rich; crystalline	Highly promising for lightweight insulation, with favourable MCC behaviour; mineral valorisation is also possible, although chloride-bearing phases require compatibility assessment with cementitious systems
RH	Bulk density: 0.1372 g cm^{-3}; porosity: 0.92; shell-derived morphology	0.0477	TGA residue: 34.4%; PHRR: 50–100 W g^{-1}; TpHRR: >350 °C	Ash yield: 15.05%; ash: highly silica-rich; predominantly amorphous	Interesting for lightweight systems with differentiated ash behaviour; possible pozzolanic interest of the ash
RS	Bulk density: 0.0275 g cm^{-3} (low); porosity: 0.97 (high); elongated fibrous morphology	0.0440	TGA residue: 31.0%; PHRR: 50–100 W g^{-1}; TpHRR: <350 °C	Ash yield: 11.15%; ash: silica-rich; mixed amorphous–crystalline	One of the strongest candidates for lightweight insulation-oriented applications; possible pozzolanic interest of the ash
SS	Bulk density: 0.0801 g cm^{-3}; porosity: 0.94; fibrous stalk-derived morphology	0.0440	TGA residue: 10.1%; PHRR: <50 W g^{-1}; TpHRR: <350 °C	Ash yield: 8.13%; ash: K- and Ca-rich; crystalline	Very interesting for lightweight insulating materials with a balanced overall profile
WS	Bulk density: 0.0895 g cm^{-3}; porosity: 0.94; elongated/cellular morphology	0.0458	TGA residue: 4.1%; PHRR: 50–100 W g^{-1}; TpHRR: <350 °C	Ash yield: 8.78%; ash: silica-rich; mixed amorphous–crystalline	Suitable for lightweight insulation-oriented uses; possible but less marked pozzolanic interest of the ash

From the perspective of lightweight building applications, the most favourable residues are those combining low apparent bulk density, high porosity, and low thermal conductivity. In this respect, luffa, rice straw, sunflower stalk, corn stalk, and *Posidonia*

oceanica define the group with the clearest insulation-oriented potential, although not all of them show the same behaviour under thermal exposure [42,44,46,47].

A second level of differentiation appears when thermal degradation and combustion-related response are considered. Among the lightweight residues, *Posidonia oceanica*, rice straw, and sunflower stalk stand out because they combine low thermal conductivity with either relatively high residual fractions after heating and/or lower combustion-related parameters. This gives them a more balanced profile within the present screening framework. By contrast, luffa represents a more contrasting case, since its very favourable insulating behaviour is not accompanied by equally low combustion-related parameters. Rice husk also defines a differentiated profile, combining low conductivity and high residual yield with comparatively high heat-release parameters [48].

The calcined fractions define additional valorisation profiles that are not directly predicted by the thermophysical results. Rice husk, rice straw, and wheat straw produce silica-rich ashes, whereas *Posidonia oceanica* is distinguished by an alkali- and Ca-rich fraction, including chloride-bearing phases such as halite and sylvite, which may represent a compatibility constraint in cementitious systems, and the olive-derived residues by more calcic or silico-calcic compositions. These profiles may guide subsequent mineral-reactivity or binder-interaction studies but do not demonstrate such performance directly.

Taken together, the most meaningful distinction among the studied residues is not simply botanical origin, but the interaction between structure, density–porosity relationship, thermal response, combustion-related behaviour, and the chemical/mineral characteristics of the ash fraction. The screening framework adopted in this study is therefore useful not for identifying a single universally optimal residue, but for distinguishing several promising candidates with different strengths depending on the intended construction application [20,59]. These results should be interpreted as preliminary criteria for prioritising candidates for subsequent composite development rather than as evidence of their final suitability or performance in construction products. The latter will also depend on application-specific factors, including binder compatibility, processing conditions, dimensional and moisture stability, biological resistance, mechanical performance, durability, and product-scale fire behaviour, which must be assessed after incorporation of the selected residues into the corresponding construction-material configurations.

4. Conclusions

This study established a first-stage comparative screening framework for ten plant-derived residues considered in supplied or minimally processed forms relevant to their potential use in bio-based construction materials. The magnitude of these differences confirms that plant-derived residues cannot be treated as a homogeneous material category. Apparent bulk density varied by approximately a factor of 30 between rice straw and olive pit, while the thermal conductivity of olive pit was approximately 2.7 times that of rice straw. For the lightweight insulation-oriented applications considered in this study, residues combining low apparent bulk density and low thermal conductivity are especially relevant because they may contribute to reducing both the weight of the resulting material and heat transfer through it. The combustion-related response was also strongly material-dependent: luffa exhibited a PHRR approximately 3.2 times that of *Posidonia oceanica*, while the residual mass after TGA was almost 18 times higher for *Posidonia oceanica* than for hemp stalk. Lower MCC heat-release parameters provide an additional favourable screening criterion, as they indicate a lower combustion hazard under the controlled conditions of the test, although they do not represent product-scale fire performance.

The combined results also showed that no individual property was sufficient for candidate selection. Low thermal conductivity was not necessarily accompanied by low

heat-release parameters, as illustrated by luffa, whereas *Posidonia oceanica*, rice straw, and sunflower stalk presented more balanced profiles for lightweight insulation-oriented development. These residues therefore appear particularly relevant as candidates for prioritisation in the subsequent development of low-density insulating composites, while materials showing more contrasted profiles may still be relevant for other construction functions or may require specific formulation strategies. The inorganic fractions were similarly differentiated, with ash yields ranging from 1.66% for olive pit to 26.23% for *Posidonia oceanica*. Rice-derived residues and wheat straw were characterised by more silica-rich ash fractions, while *Posidonia oceanica* exhibited a distinctive Na- and Ca-rich oxide profile together with chloride-bearing halite identified by XRD, indicating different mineral characteristics that should be considered in subsequent material development or ash valorisation.

The characterisation performed here does not demonstrate the final suitability or performance of finished construction products. Its contribution lies in reducing the experimental space associated with the large number of possible residues, binders, formulations, and manufacturing conditions by identifying candidates with differentiated and potentially complementary profiles. Subsequent work must validate these findings through composite manufacture and application-level assessment, including binder compatibility, processability, dimensional and moisture stability, mechanical performance, biological resistance, durability, and product-scale fire behaviour.

Author Contributions: B.A.-C.: writing—review and editing, writing—original draft preparation, software, resources, methodology, investigation, funding acquisition, formal analysis, data curation, conceptualisation. A.M.L.: writing—review and editing, validation, supervision, resources, project administration, funding acquisition, data curation, conceptualisation. L.H.: writing—review nd editing, validation, supervision, resources, project administration, funding acquisition, formal analysis, data curation, conceptualisation. A.N.-E.: validation, supervision, formal analysis, investigation, conceptualisation. All authors have read and agreed to the published version of the manuscript.

Funding: This work was partially funded by MICIU/AEI/10.13039/501100011033 through the project PID2020-117530RB-I00. The authors also acknowledge the financial support provided to the research group GICITED by AGAUR (2021 SGR 01405). The first author gratefully acknowledges the financial support of the Spanish Minister scholarship: "Subprograma Estatal de Formación del Programa Estatal para Desarrollar, Atraer y Retener Talento, en el marco del Plan Estatal de Investigación Científica".

Data Availability Statement: The original contributions presented in this study are included in the article. Further inquiries can be directed to the corresponding author.

Conflicts of Interest: The authors declare no conflicts of interest.

Abbreviations

The following abbreviations are used in this manuscript:

CS	Corn Stalk
HS	Hemp Stalk
Lu	Luffa
OB	Olive Branches
OP	Olive Pit
PO	Posidonia Oceanica
RH	Rice Husk
RS	Rice Straw
SS	Sunflower Stalk
WS	Wheat Straw

SD	Standard Deviation
SEM	Scanning Electron Microscopy
SEM-EDS	Energy-Dispersive X-ray Spectroscopy
TGA	Thermogravimetric Analysis
DTG	Derivative Thermogravimetry
MCC	Microscale Combustion Calorimetry
FTIR	Fourier Transform Infrared Spectroscopy
XRF	X-Ray Fluorescence
XRD	X-Ray Diffraction
Phrr	Peak Heat Release Rate
Tphrr	Temperature At Peak Heat Release Rate
THR	Total Heat Release
HRC	Heat Release Capacity

References

1. United Nations Environment Programme; Global Alliance for Buildings and Construction. *Global Status Report for Buildings and Construction 2025–2026: As Climate Risks Rise and Cities Grow, We Must Rethink How We Build to Create Better Lives for All*; UNEP: Paris, France, 2026. [CrossRef]
2. Bourbia, S.; Kazeoui, H.; Belarbi, R. A review on recent research on bio-based building materials and their applications. *Mater. Renew. Sustain. Energy* **2023**, *12*, 117–139. [CrossRef]
3. Schiavoni, S.; D'Alessandro, F.; Bianchi, F.; Asdrubali, F. Insulation materials for the building sector: A review and comparative analysis. *Renew. Sustain. Energy Rev.* **2016**, *62*, 988–1011. [CrossRef]
4. Cintura, E.; Nunes, L.; Esteves, B.; Faria, P. Agro-industrial wastes as building insulation materials: A review and challenges for Euro-Mediterranean countries. *Ind. Crops Prod.* **2021**, *171*, 113833. [CrossRef]
5. Liuzzi, S.; Sanarica, S.; Stefanizzi, P. Use of agro-wastes in building materials in the Mediterranean area: A review. *Energy Procedia* **2017**, *126*, 242–249. [CrossRef]
6. Asdrubali, F.; D'Alessandro, F.; Schiavoni, S. A review of unconventional sustainable building insulation materials. *Sustain. Mater. Technol.* **2015**, *4*, 1–17. [CrossRef]
7. Bumanis, G.; Irbe, I.; Sinka, M.; Bajare, D. Biodeterioration of sustainable hemp shive biocomposite based on gypsum and phosphogypsum. *J. Nat. Fibers* **2022**, *19*, 10550–10563. [CrossRef]
8. Amziane, S.; Collet, F.; Lawrence, M.; Magniont, C.; Picandet, V.; Sonebi, M. Recommendation of the RILEM TC 236-BBM: Characterisation testing of hemp shiv to determine the initial water content, water absorption, dry density, particle size distribution and thermal conductivity. *Mater. Struct.* **2017**, *50*, 167. [CrossRef]
9. Glé, P.; Gourdon, E.; Arnaud, L. Modelling of the acoustical properties of hemp particles. *Constr. Build. Mater.* **2012**, *37*, 801–811. [CrossRef]
10. Okeke, F.O.; Ahmed, A.; Imam, A.; Hassanin, H. A review of corncob-based building materials as a sustainable solution for the building and construction industry. *Hybrid Adv.* **2024**, *6*, 100269. [CrossRef]
11. Kulshreshtha, Y.; Schlangen, E.; Jonkers, H.; Vardon, P.; van Paassen, L. CoRncrete: A corn starch based building material. *Constr. Build. Mater.* **2017**, *154*, 411–423. [CrossRef]
12. Bovo, M.; Giani, N.; Barbaresi, A.; Mazzocchetti, L.; Barbaresi, L.; Giorgini, L.; Torreggiani, D.; Tassinari, P. Contribution to thermal and acoustic characterization of corn cob for bio-based building insulation applications. *Energy Build.* **2022**, *262*, 111994. [CrossRef]
13. de la Casa, J.A.; Bueno, J.S.; Castro, E. Recycling of residues from the olive cultivation and olive oil production process for manufacturing of ceramic materials. A comprehensive review. *J. Clean. Prod.* **2021**, *296*, 126436. [CrossRef]
14. Donner, M.; Erraach, Y.; López-I-Gelats, F.; Manuel-I-Martin, J.; Yatribi, T.; Radić, I.; El Hadad-Gauthier, F. Circular bioeconomy for olive oil waste and by-product valorisation: Actors' strategies and conditions in the Mediterranean area. *J. Environ. Manag.* **2022**, *321*, 115836. [CrossRef]
15. Palumbo, M.; Lacasta, A.; Giraldo, M.; Haurie, L.; Correal, E. Bio-based insulation materials and their hygrothermal performance in a building envelope system (ETICS). *Energy Build.* **2018**, *174*, 147–155. [CrossRef]
16. Khoukhi, M.; Saleh, A.D.; Mohammad, A.F.; Hassan, A.; Abdelbaqi, S. Thermal performance and statistical analysis of a new bio-based insulation material produced using grain puffing technique. *Constr. Build. Mater.* **2022**, *345*, 128311. [CrossRef]
17. Arufe, S.; de Menibus, A.H.; Leblanc, N.; Lenormand, H. Physico-chemical characterisation of plant particles with potential to produce biobased building materials. *Ind. Crops Prod.* **2021**, *171*, 113901. [CrossRef]

18. Viel, M.; Collet, F.; Lanos, C. Chemical and multi-physical characterization of agro-resources' by-product as a possible raw building material. *Ind. Crops Prod.* **2018**, *120*, 214–237. [CrossRef]
19. Yang, Y.; Haurie, L.; Wang, D.-Y. Bio-based materials for fire-retardant application in construction products: A review. *J. Therm. Anal. Calorim.* **2022**, *147*, 6563–6582. [CrossRef]
20. Vassilev, S.V.; Baxter, D.; Vassileva, C.G. An overview of the behaviour of biomass during combustion: Part I. Phase-mineral transformations of organic and inorganic matter. *Fuel* **2013**, *112*, 391–449. [CrossRef]
21. Avellaneda, A.; Evon, P.; Haurie, L.; Laborel-Préneron, A.; Lagouin, M.; Magniont, C.; Navarro, A.; Palumbo, M.; Torres, A. Evaluation of the Potential of Plant Aggregates from Corn and Sunflower Stalks for the Design of Building Materials. In *Bio-Based Building Materials, Proceedings of ICBBM 2023*; Amziane, S., Merta, I., Page, J., Eds.; Springer: Cham, Switzerland, 2023; Volume 45, pp. 70–86. [CrossRef]
22. Martínez, B.; Bernat-Maso, E.; Gil, L. Applications and properties of hemp stalk-based insulating biomaterials for buildings: Review. *Materials* **2023**, *16*, 3245. [CrossRef]
23. Mati-Baouche, N.; De Baynast, H.; Lebert, A.; Sun, S.; Lopez-Mingo, C.J.S.; Leclaire, P.; Michaud, P. Mechanical, thermal and acoustical characterizations of an insulating bio-based composite made from sunflower stalks particles and chitosan. *Ind. Crops Prod.* **2014**, *58*, 244–250. [CrossRef]
24. Hussein, Z.; Ashour, T.; Khalil, M.; Bahnasawy, A.; Ali, S.; Hollands, J.; Korjenic, A. Rice straw and flax fiber particleboards as a product of agricultural waste: An evaluation of technical properties. *Appl. Sci.* **2019**, *9*, 3878. [CrossRef]
25. Norford, L.K.; Glicksman, L.R.; Harvey, H.S.; Charlson, J.A. Development of low-cost wheat-straw insulation board. *HVAC R Res.* **1999**, *5*, 249–263. [CrossRef]
26. Peceño, B.; Perez-Soriano, E.M.; Ríos, J.D.; Luna-Galiano, Y.; Cifuentes, H.; Fernández, C.L. Morphological analysis of porosity and sound absorption in sustainable materials from rice husk. *Build. Acoust.* **2022**, *29*, 387–399. [CrossRef]
27. Halashi, K.; Taban, E.; Soltani, P.; Amininasab, S.; Samaei, E.; Moghadam, D.N.; Khavanin, A. Acoustic and thermal performance of luffa fiber panels for sustainable building applications. *Build. Environ.* **2024**, *247*, 111051. [CrossRef]
28. de Madrid, U.P.; Rodríguez, J.G.; Martínez, F.F.; Astorqui, J.S.C. Viability of using olive stones as lightweight aggregate in construction mortars. *Rev. DE LA Constr.* **2017**, *16*, 431–438. [CrossRef]
29. Liuzzi, S.; Rubino, C.; Stefanizzi, P. Use of clay and olive pruning waste for building materials with high hygrothermal performances. *Energy Procedia* **2017**, *126*, 234–241. [CrossRef]
30. Glé, P.; Lecompte, T.; de Ménibus, A.H.; Lenormand, H.; Arufe, S.; Chateau, C.; Fierro, V.; Celzard, A. Densities of hemp shiv for building: From multiscale characterisation to application. *Ind. Crops Prod.* **2021**, *164*, 113390. [CrossRef]
31. Palumbo, M.; Alva, A.; Haurie, L.; Avellaneda, A.; Lacasta, A.M. Full-scale prototype wall systems incorporating agricultural bio-based materials: Design, construction, first results of an in-situ monitoring campaign, and preliminary dynamic thermal and acoustic analysis. *J. Build. Eng.* **2026**, *130*, 117062. [CrossRef]
32. Palumbo, M.; Alva, A.; Lacasta, A.M.; Lagouin, M.; Haurie, L.; Avellaneda, A.; Alam, B.; Laborel-Préneron, A.; Magniont, C. Upcycling sunflower pith as a sustainable bio-aggregate for circular insulation systems: A thermal, acoustic, and fire performance assessment. *Constr. Build. Mater.* **2026**, *535*, 146806. [CrossRef]
33. Ratsimbazafy, H.H.; Laborel-Préneron, A.; Magniont, C.; Evon, P. A review of the multi-physical characteristics of plant aggregates and their effects on the properties of plant-based concrete. *Recent Prog. Mater.* **2021**, *3*, 026. [CrossRef]
34. Laborel-Préneron, A.; Aubert, J.E.; Magniont, C.; Tribout, C.; Bertron, A. Plant aggregates and fibers in earth construction materials: A review. *Constr. Build. Mater.* **2016**, *111*, 719–734. [CrossRef]
35. Amziane, S.; Sonebi, M. Overview on biobased building material made with plant aggregate. *RILEM Tech. Lett.* **2016**, *1*, 31–38. [CrossRef]
36. Schneider, C.A.; Rasband, W.S.; Eliceiri, K.W. NIH Image to ImageJ: 25 years of image analysis. *Nat. Methods* **2012**, *9*, 671–675. [CrossRef]
37. Applied Precision Ltd. ISOMET 2114: Portable Hand-Held Measuring Instrument for Direct Measurement of Heat Transfer Properties. Available online: https://www.appliedp.com/product/isomet/ (accessed on 13 May 2026).
38. Alshammari, B.A.; Alotaibi, M.D.; Alothman, O.Y.; Sanjay, M.R.; Kian, L.K.; Almutairi, Z.; Jawaid, M. A new study on characterization and properties of natural fibers obtained from olive tree (*Olea europaea* L.) residues. *J. Polym. Environ.* **2019**, *27*, 2334–2340. [CrossRef]
39. *ASTM D7309-21b*; Standard Test Method for Determining Flammability Characteristics of Plastics and Other Solid Materials Using Microscale Combustion Calorimetry. ASTM International: West Conshohocken, PA, USA, 2021. [CrossRef]
40. Ramírez-Hernández, A.; Aguilar-Flores, C.; Aparicio-Saguilán, A. Fingerprint analysis of FTIR spectra of polymers containing vinyl acetate. *DYNA* **2019**, *86*, 198–205. [CrossRef]
41. Cosentino, L.; Fernandes, J.; Mateus, R. A review of natural bio-based insulation materials. *Energies* **2023**, *16*, 4676. [CrossRef]
42. Ali, A.; Issa, A.; Elshaer, A. A comprehensive review and recent trends in thermal insulation materials for energy conservation in buildings. *Sustainability* **2024**, *16*, 8782. [CrossRef]

43. Climate Technology Centre and Network. Building Envelope Thermal Insulation—Energy Efficiency. Available online: https://www.ctc-n.org/technologies/building-envelope-thermal-insulation (accessed on 16 June 2026).
44. Petcu, C.; Hegyi, A.; Stoian, V.; Dragomir, C.S.; Ciobanu, A.A.; Lăzărescu, A.-V.; Florean, C. Research on thermal insulation performance and impact on indoor air quality of cellulose-based thermal insulation materials. *Materials* **2023**, *16*, 5458. [CrossRef]
45. Grazieschi, G.; Asdrubali, F.; Thomas, G. Embodied energy and carbon of building insulating materials: A critical review. *Clean. Environ. Syst.* **2021**, *2*, 100032. [CrossRef]
46. Rocha, B.M.; Tenório, M.; Branco, J.M.; Silva, S.M. A comprehensive comparison of insulation materials for timber building systems. *Energies* **2025**, *18*, 2420. [CrossRef]
47. Ye, F.; Wei, H.; Xiao, Y.; Berardi, U.; Quaranta, G.; Demartino, C. Bio-based insulation materials in sustainable constructions: A review of environmental, thermal and acoustic insulation, durability, and mechanical performances. *Renew. Sustain. Energy Rev.* **2025**, *223*, 115872. [CrossRef]
48. Varol, E.A.; Mutlu, Ü. TGA-FTIR analysis of biomass samples based on the thermal decomposition behavior of hemicellulose, cellulose, and lignin. *Energies* **2023**, *16*, 3674. [CrossRef]
49. Yang, H.; Yan, R.; Chen, H.; Lee, D.H.; Zheng, C. Characteristics of hemicellulose, cellulose and lignin pyrolysis. *Fuel* **2007**, *86*, 1781–1788. [CrossRef]
50. Várhegyi, G.; Bobály, B.; Jakab, E.; Chen, H. Thermogravimetric study of biomass pyrolysis kinetics. A distributed activation energy model with prediction tests. *Energy Fuels* **2011**, *25*, 24–32. [CrossRef]
51. Carrier, M.; Loppinet-Serani, A.; Denux, D.; Lasnier, J.-M.; Ham-Pichavant, F.; Cansell, F.; Aymonier, C. Thermogravimetric analysis as a new method to determine the lignocellulosic composition of biomass. *Biomass Bioenergy* **2011**, *35*, 298–307. [CrossRef]
52. Xu, Q.; Mensah, R.A.; Jin, C.; Jiang, L. A critical review of the methods and applications of microscale combustion calorimetry for material flammability assessment. *J. Therm. Anal. Calorim.* **2022**, *147*, 6001–6013. [CrossRef]
53. Mensah, R.A.; Xu, Q.; Asante-Okyere, S.; Jin, C.; Bentum-Micah, G. Correlation analysis of cone calorimetry and microscale combustion calorimetry experiments. *J. Therm. Anal. Calorim.* **2019**, *136*, 589–599. [CrossRef]
54. Lowden, L.A.; Hull, T.R. Flammability behaviour of wood and a review of the methods for its reduction. *Fire Sci. Rev.* **2013**, *2*, 4. [CrossRef]
55. Heredia-Guerrero, J.A.; Benítez, J.J.; Domínguez, E.; Bayer, I.S.; Cingolani, R.; Athanassiou, A.; Heredia, A. Infrared and Raman spectroscopic features of plant cuticles: A review. *Front. Plant Sci.* **2014**, *5*, 305. [CrossRef]
56. Morán, J.I.; Alvarez, V.A.; Cyras, V.P.; Vázquez, A. Extraction of cellulose and preparation of nanocellulose from sisal fibers. *Cellulose* **2008**, *15*, 149–159. [CrossRef]
57. Islam, M.S.; Hasan, M.; Ahmad, M.B. Chemical Modification and Properties of Cellulose-Based Polymer Composites. In *Lignocellulosic Polymer Composites: Processing, Characterization, and Properties*; Thakur, V.K., Ed.; Wiley: Hoboken, NJ, USA, 2014; pp. 301–324. [CrossRef]
58. Jayamani, E.; Loong, T.G.; Bakri, M.K.B. Comparative study of Fourier transform infrared spectroscopy (FTIR) analysis of natural fibres treated with chemical, physical and biological methods. *Polym. Bull.* **2020**, *77*, 1605–1629. [CrossRef]
59. Sommersacher, P.; Brunner, T.; Obernberger, I. Fuel indexes: A novel method for the evaluation of relevant combustion properties of new biomass fuels. *Energy Fuels* **2012**, *26*, 380–390. [CrossRef]
60. Angst, U.; Elsener, B.; Larsen, C.K.; Vennesland, Ø. Critical chloride content in reinforced concrete—A review. *Cem. Concr. Res.* **2009**, *39*, 1122–1138. [CrossRef]
61. Sui, S.; Wang, F.; Wu, M.; Li, S.; Liu, Z.; Gao, S.; Jiang, J. Influence of sodium chloride on the hydration of C3S blended paste. *Constr. Build. Mater.* **2023**, *369*, 130543. [CrossRef]
62. Rajabipour, F.; Giannini, E.; Dunant, C.; Ideker, J.H.; Thomas, M.D.A. Alkali–silica reaction: Current understanding of the reaction mechanisms and the knowledge gaps. *Cem. Concr. Res.* **2015**, *76*, 130–146. [CrossRef]

Disclaimer/Publisher's Note: The statements, opinions and data contained in all publications are solely those of the individual author(s) and contributor(s) and not of MDPI and/or the editor(s). MDPI and/or the editor(s) disclaim responsibility for any injury to people or property resulting from any ideas, methods, instructions or products referred to in the content.